Environmental Modelling and Software 153 (2022) 105386

Contents lists available at ScienceDirect

Environmental Modelling and Software

journal homepage: www.elsevier.com/locate/envsoft

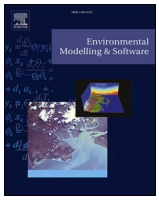

HyPix: 1D physically based hydrological model with novel adaptive time-stepping management and smoothing dynamic criterion for controlling Newton–Raphson step

J.A.P. Pollacco [a], J. Fernández-Gálvez [b,a,1,*], P. Ackerer [c], B. Belfort [c], L. Lassabatere [d], R. Angulo-Jaramillo [d], C. Rajanayaka [e], L. Lilburne [a], S. Carrick [a], D.A. Peltzer [a]

[a] Manaaki Whenua – Landcare Research, Lincoln, New Zealand
[b] Department of Regional Geographic Analysis and Physical Geography, University of Granada, Spain
[c] Université de Strasbourg, CNRS/EOST, ITES UMR, 7063, Institut Terre et Environnement de Strasbourg, Strasbourg, France
[d] Univ Lyon, Université Claude Bernard Lyon 1, CNRS, ENTPE, UMR5023 LEHNA, Vaulx en Velin, Lyon, France
[e] National Institute of Water and Atmospheric Research, Christchurch, New Zealand

ARTICLE INFO

Keywords:
Richardson–Richards' equation
Unsaturated porous media
Variably saturated flow
Time-stepping manager
Newton–Raphson step
Julia language

ABSTRACT

The newly developed open-source **Hy**drological **Pix**el model, HyPix, written in the fast and flexible Julia language, efficiently solves the mixed form of the Richardson–Richards' equation (RRE). HyPix uses a *cell-centred, finite-volume* scheme for the spatial discretization, with an *implicit Euler scheme* for the temporal discretization, by using the *weighted average* inter-cell hydraulic conductivity. HyPix includes the following modules: **(a)** *rainfall interception*, **(b)** *root water uptake* with compensation algorithm and root growth, **(c)** *soil evaporation*, **(d)** *ponding* using a novel method for computing *sorptivity*, and **(e)** *runoff*. HyPix includes a wide range of top and boundary conditions (*flux, pressure, free drainage*). To control the Newton–Raphson iterations, HyPix incorporates a novel dynamic physical smoothing criterion, which improves not only the model performance but also its accuracy compared with using the traditional absolute convergence criterion. To control the time-step, the traditional physical time-step management based on changes in the soil water content was specifically designed to solve RRE based on soil water content. This work adapts the time-step management such that it is specifically designed to solve RRE based on soil water pressure without introducing further parameters. The novel time-step management also requires only one parameter and was found to be more efficient than the traditional time-step management. HyPix implements an option to solve the derivatives numerically, enabling the RRE to be modified and tested (e.g., the inter-cell hydraulic conductivity) by changing only a few lines of code. Numerically calculating derivatives was found to be as accurate as deriving the derivatives analytically, and only 10–25% slower.

The well-established hydrological model HYDRUS was used to validate HyPix without the sink term. The HyPix results show good agreement to HYDRUS, validating the algorithms implemented in HyPix. Even for challenging conditions, HyPix can provide accurate and reliable results using the recommended standard options. Moreover, the algorithm developed in HyPix is more efficient than the one used in HYDRUS, particularly for coarse texture soils. The recommended options were also tested by running HyPix with sink term using field data.

1. Introduction

Understanding and modelling processes within the critical zone, extending from the top of the vegetation canopy to the lower limit of groundwater, are of great importance for better managing and protecting water resources (e.g., Ranatunga et al., 2008) under increasing demands and changing climatic conditions (National Research Council, 2001). The vadose zone holds a central position in this complex system, governed by numerous interactions. As a result, the development of robust and efficient numerical solutions describing

* Corresponding author.
E-mail address: jesusfg@ugr.es (J. Fernández-Gálvez).
[1] Permanent address: Department of Regional Geographic Analysis and Physical Geography, University of Granada, Spain.

https://doi.org/10.1016/j.envsoft.2022.105386
Received 17 January 2022; Received in revised form 23 March 2022; Accepted 27 March 2022
Available online 22 April 2022

water flows in unsaturated porous media remains a challenge that is relevant to a wide range of scientists, agricultural applications, and policy makers.

The Richardson-Richards' equation (RRE, Richardson, 1922; Richards, 1931), usually known as Richards' equation, which combines the continuity equation with Darcy–Buckingham's (DB) law, provides a physical basis for modelling the water movement through the unsaturated zone (e.g., Farthing and Ogden, 2017; Raats, 2001). Hence, it is implemented in many distributed hydrological models at watershed or regional scales (e.g., Shen and Phanikumar, 2010), and also in land surface models that often represent the vertical water movement in the soil through the 1D-RRE (e.g., Bisht et al., 2018; Dai et al., 2019). A key condition to validate this approach remains the existence of a local scale for which DB law is valid and suitable physical parameters can be provided for the constitutive relationships describing the $K(\psi)$, hydraulic conductivity [L T^{-1}], and $\theta(\psi)$, volumetric water content [L^3 L^{-3}], functions of the soil water pressure ψ [L]. Since highly non-linear parametric models are generally used to describe these interdependent relationships, the RRE must be solved numerically because there is no exact analytical solution. This means that modellers are burdened with solving a non-linear partial differential equation potentially varying between a hyperbolic to a parabolic mathematical form depending on the soil condition. All things considered, the numerical solution of the RRE is one of the most challenging problems in earth sciences, with a high risk of non-convergence (e.g., Farthing and Ogden, 2017).

Advanced numerical schemes well suited to handling complex spatial grids (e.g., Qi et al., 2018) and optimized time discretization procedures are available to solve the different forms of the RRE (Fahs et al., 2009; Farthing and Ogden, 2017; Maina and Ackerer, 2017). To briefly summarize the current situation, the *θ-form* of the RRE provides excellent mass balance but cannot handle water flows in saturated zones and exhibits discontinuities in the dependent variable across soil layer boundaries. On the other hand, the *ψ-form* is continuous in both saturated and unsaturated zones but can suffer large mass balance errors (Celia et al., 1990; Hills et al., 1989). Finally, the RRE is often presented and solved using the mixed form, and the computational codes usually contain a step where the primary variable is chosen to linearize and solve the mathematical system, which then updates secondary variables. Very efficient results have been obtained with variable switching methods. These consist of selecting the primary variable to be computed (i.e., θ or ψ) for each node of the matrix system as a function of the saturation of the soil (Diersch and Perrochet, 1999; Forsyth et al., 1995; Wu and Forsyth, 2001). Improvements, especially for non-smooth transitions between alternative primary variables, have been developed to prevent unrealistic solutions or numerical difficulties (Krabbenhøft, 2007; Lehmann and Ackerer, 1998; Zha et al., 2017).

The temporal discretization usually proceeds with an implicit scheme, and the resulting non-linear algebraic system requires an efficient and robust linearization technique that maintains mass conservation and accuracy of the solution. The Picard and Newton–Raphson (NR) iterative methods are the most widely used procedures for solving the RRE. Due to its robustness and simplicity, the Picard method is more widespread and has been, for instance, implemented in several popular numerical codes solving the RRE, such as the HYDRUS (Šimůnek et al., 2016) and SWAP (van Dam et al., 2008) models. Nonetheless, slow or no convergence have been encountered with this technique for cases of saturated–unsaturated interfaces, gravity drainage, or complex time-varying boundary conditions (Paniconi et al., 1991). The NR method has been found to be more efficient than the Picard iteration method (Miller et al., 1998; Paniconi et al., 1991; Paniconi and Putti, 1994), but it increases algebraic complexity and computational costs because of the Jacobian matrix containing some derivative terms and leading to a non-symmetric matrix system (Paniconi and Putti, 1994).

Convergence failure of the NR method can occur in some unfavourable flow conditions, especially when simulating infiltration into initially dry soils where the head gradient at the wetting front is extremely large. To solve this numerical difficulty, Zha et al. (2019) proposed an algorithm where the ψ before and after the iteration are examined. The proposed modifications do not degrade the simulated results, leading to more robust convergence performances and cost-effective simulations for this particularly challenging conditions. Alternatively, efficient non-iterative techniques can also be implemented (Kavetski et al., 2002; Li et al., 2021).

Finally, linked with the linearization technique and the spatial discretization scheme, the numerical solution of the RRE can be sensitive to the convergence-control strategies and the method to adapt the time-step size during the simulation. Compared to using a fixed time-step, adaptive time discretization is more efficient and has become quite common, ranging from heuristic to control-based-error methods. A large number of heuristic time-stepping methods have been proposed in the literature (e.g., Thomas and Gladwell, 1988; Kavetski et al., 2001; Kavetski and Binning, 2004; Miller et al., 2006; Belfort et al., 2007).

A key aspect justifying ongoing research of improvements relies on the need to balance run time, robustness, accuracy, and flexibility. Despite numerous efforts over the last decade, algorithms to achieve fast and accurate solutions are still actively being researched (e.g., Zha et al., 2019). Here, we propose improvements to the solution of the RRE and implement them in the novel **Hy**drological **Pix**el (HyPix) model using the mixed form of the RRE. The solution of the RRE is based on Maina and Ackerer (2017), for which the RRE partial differential equation is solved using a *cell-centred finite-volume* (implicit finite differences) scheme for the spatial discretization, with an *implicit Euler scheme* for the temporal discretization by using the *weighted average* inter-cell hydraulic conductivity. Then, HyPix solves the mixed form of the RRE using the NR method.

To avoid overshooting and losing control of the NR step, we propose a new physical method which automatically controls the convergence rate depending on the difficulty to get the solution. As previously mentioned, the drawback of solving the RRE with the NR method is that it requires reprogramming the computation of the Jacobian matrices (i.e., the derivatives of the parameters with respect to ψ); hence for testing purposes, changing inter-cell hydraulic conductivities leads to a reprogramming of the derivatives. To overcome this limitation, HyPix takes advantage of the Julia language (Bezanson et al., 2017; Perkel, 2019), which enables automatic resolution of derivatives (Revels et al., 2016).

An updated physical time-stepping scheme has been developed that is tailored to solve the RRE based on ψ (and not θ) without introducing additional parameters. The time-stepping management module optimizes the size of the time-step, ΔT, such that HyPix uses the largest ΔT while meeting the targeted water balance and accuracy of the solution. Our technique is adapted from Kirkland et al. (1992) and Ross (2003), because their time-stepping management is physically based, such that ΔT is directly derived from the residuals of the water balance and requires fitting of only one physical parameter. ΔT is calculated via a maximum increase or decrease of the degree of saturation for each cell; this ensures a higher time resolution when θ variations are large, which improves the convergence rate at the wetting front.

The newly developed model has a reduced number of parameters to manage the solving of the RRE compared to other physically based

hydrological models. HyPix can **(a)** process a large number of soil layers described by the Kosugi (1994, 1996) unimodal and bimodal *K(ψ)* and *θ(ψ)* hydraulic parameters for each soil layer, **(b)** simulate for the top boundary condition realistic water *ponding* and *runoff* at the soil surface by using a novel approach for the computation of *sorptivity*, **(c)** compute root water uptake and *evaporation*, **(d)** apply a wide range of bottom boundary conditions such as prescribed bottom flux or pressure (i.e., water table), free drainage, and impermeable layer; and **(e)** model impermeable layers.

This paper is organized as follows: section 2 presents the bimodal soil Kosugi hydraulic functions used in HyPix, to describe the RRE and the novel approaches to solve it; section 3 presents the five synthetic test cases used to validate HyPix with HYDRUS and the experimental data from five field sites; section 4 presents the results of comparing HYDRUS with HyPix and the performance of different HyPix option used with field experimental data; section 5 discusses the results of the best HyPix options based on synthetic and field experimental data; and section 6 summarizes the main conclusions.

2. Theory

2.1. Bimodal Kosugi soil hydraulic functions

$$\begin{cases} \theta(\psi) = \theta_{\mathrm{Mat}}(\psi) + \theta_{\mathrm{Mac}}(\psi) \\ \textbf{if } \psi \leqslant 0 \\ \theta_{\mathrm{Mat}}(\psi) = \dfrac{1}{2}[\theta_{s\mathrm{MacMat}} - \theta_r]\mathrm{erfc}\left[\dfrac{\ln\left(-\psi/\psi_m\right)}{\sqrt{2}\,\sigma}\right] + \theta_r \\ \theta_{\mathrm{Mac}}(\psi) = \dfrac{1}{2}[\theta_s - \theta_{s\mathrm{MacMat}}]\mathrm{erfc}\left[\dfrac{\ln\left(-\psi/\psi_{m\mathrm{Mac}}\right)}{\sqrt{2}\,\sigma_{\mathrm{Mac}}}\right] \\ \textbf{elseif } \psi > 0 \\ \theta_{\mathrm{Mat}}(\psi) = \theta_{s\mathrm{MacMat}} \\ \theta_{\mathrm{Mac}}(\psi) = \theta_s - \theta_{s\mathrm{MacMat}} \end{cases} \tag{1}$$

$$\begin{cases} K(\psi) = K_{\mathrm{Mat}}(S_e(\psi)) + K_{\mathrm{Mac}}(S_e(\psi)) \\ \textbf{if } \psi \leqslant 0 \\ S_e(\psi) = \dfrac{\theta - \theta_r}{\theta_s - \theta_r} = \dfrac{1}{2}\left[\dfrac{\theta_{s\mathrm{MacMat}} - \theta_r}{\theta_s - \theta_r}\mathrm{erfc}\left[\dfrac{\ln\left(-\psi/\psi_m\right)}{\sqrt{2}\,\sigma}\right] + \dfrac{\theta_s - \theta_{s\mathrm{MacMat}}}{\theta_s - \theta_r}\mathrm{erfc}\left[\dfrac{\ln\left(-\psi/\psi_{m\mathrm{Mac}}\right)}{\sqrt{2}\,\sigma_{\mathrm{Mac}}}\right]\right] \\ K_{\mathrm{Mat}}(S_e(\psi)) = K_s\dfrac{\theta_{s\mathrm{MacMat}} - \theta_r}{\theta_s - \theta_r}\sqrt{S_e(-\psi)}\left[\dfrac{1}{2}\mathrm{erfc}\left[\dfrac{\ln\left(-\psi/\psi_m\right)}{\sqrt{2}\,\sigma} + \dfrac{\sigma}{\sqrt{2}}\right]\right]^2 \\ K_{\mathrm{Mac}}(S_e(\psi)) = K_s\dfrac{\theta_s - \theta_{s\mathrm{MacMat}}}{\theta_s - \theta_r}\sqrt{S_e(-\psi)}\left[\dfrac{1}{2}\mathrm{erfc}\left[\dfrac{\ln\left(-\psi/\psi_{m\mathrm{Mac}}\right)}{\sqrt{2}\,\sigma_{\mathrm{Mac}}} + \dfrac{\sigma_{\mathrm{Mac}}}{\sqrt{2}}\right]\right]^2 \\ \textbf{elseif } \psi > 0 \\ K_{\mathrm{Mat}}(S_e(\psi)) = K_s\dfrac{\theta_{s\mathrm{MacMat}} - \theta_r}{\theta_s - \theta_r} \\ K_{\mathrm{Mac}}(S_e(\psi)) = K_s\dfrac{\theta_s - \theta_{s\mathrm{MacMat}}}{\theta_s - \theta_r} \end{cases} \tag{2}$$

HyPix uses the bimodal Kosugi (1994, 1996) soil hydraulic functions. The choice of the Kosugi soil hydraulic functions is based on the physical interpretation of their parameters in relation to the soil pore size distribution. The Kosugi hydraulic parameters can be physically interpreted and constrained by exploiting physical relationship between the parameters (Fernández-Gálvez et al., 2021; Pollacco et al., 2013b). Moreover, the selection of bimodal functions is based on the prevalence of soils with bimodal pore system (e.g., Jarvis, 2007; McLeod et al., 2008), where macropores and micropores lead to two-stage drainage. Fast flow (macropore flow) can occur when the water pressure head exceeds the threshold needed to activate the macropore network, adding to the matrix flow. Below this threshold, only the matrix participates in the flow (Fernández-Gálvez et al., 2021). The representation of the *θ(ψ)* and *K(ψ)* functions is based on the dual porosity model of Pollacco et al. (2017):

where erfc is the complementary error function; θ [$L^3\ L^{-3}$] represents the *volumetric soil water content* and ψ [L] the *soil water pressure*, considering $\psi < 0$ for unsaturated soils (i.e., *matrix suction*); θ_s [$L^3\ L^{-3}$] and θ_r [$L^3\ L^{-3}$] are the *saturated* and *residual volumetric soil water content*, respectively; ln ψ_m and σ [-] denote the mean and standard deviation of ln ψ, respectively, in the soil matrix domain; ln $\psi_{m\mathrm{Mac}}$ and σ_{Mac} [-] denote the mean and standard deviation of ln ψ, respectively, in the macropore soil domain (with the argument of ln in units of length, i.e., ψ_m, ψ, and $\psi_{m\mathrm{Mac}}$ in [L]); $\theta_{s\mathrm{MacMat}}$ [$L^3\ L^{-3}$] is the volumetric saturated water content that theoretically differentiates inter-aggregate pores (structural macropores) and matrix domains (intra-aggregate micropores), defining the corresponding soil water pressure threshold between macropore and matrix ψ_{MacMat} [L]; $S_e(\psi)$ [-] denotes the *effective saturation* as a function of ψ with values between 0 and 1; K_s [$L\ T^{-1}$] is the *saturated hydraulic conductivity*; and $K(S_e(\psi))$ [$L\ T^{-1}$] refers to the

unsaturated hydraulic conductivity, written as a function of $S_e(\psi)$. For the case when $\theta_{sMacMat} = \theta_s$, Eq. (1) and Eq. (2) reduce to the unimodal Kosugi soil hydraulic functions.

if $\psi \leqslant 0$

$$C(\theta,\psi) = \frac{\partial\theta}{\partial\psi} = \frac{\partial\theta_{\mathrm{Mat}}}{\partial\psi} + \frac{\partial\theta_{\mathrm{Mac}}}{\partial\psi} = -[\theta_{sMatMac} - \theta_r]\frac{\exp\left[\frac{-\left[\ln\left(-\psi/\psi_m\right)\right]^2}{2\sigma^2}\right]}{\sqrt{2\pi}\sigma^2 - \psi} - [\theta_s - \theta_{sMatMac}]\frac{\exp\left[\frac{-\left[\ln\left(-\psi/\psi_{mMac}\right)\right]^2}{2\sigma_{\mathrm{Mac}}^2}\right]}{\sqrt{2\pi}\sigma_{\mathrm{Mac}} - \psi} \tag{3}$$

elseif $\psi > 0$

$C(\theta,\psi) = 0$

The soil water capacity of the bimodal Kosugi model is computed as follow:

And the derivative of $K(\psi)$ with respect to ψ of the bimodal Kosugi model is:

$$\begin{cases}
\dfrac{\partial K}{\partial\psi} = \dfrac{\partial K_{\mathrm{Mat}}}{\partial\psi} + \dfrac{\partial K_{\mathrm{Mac}}}{\partial\psi} \\
\textbf{if } \psi \leqslant 0 \\
S_e(\psi) = \dfrac{\theta - \theta_r}{\theta_s - \theta_r} = \dfrac{1}{2}\left[\dfrac{\theta_{sMacMat} - \theta_r}{\theta_s - \theta_r}\mathrm{erfc}\left[\dfrac{\ln\psi/\psi_m}{\sqrt{2}\,\sigma}\right] + \dfrac{\theta_s - \theta_{sMacMat}}{\theta_s - \theta_r}\mathrm{erfc}\left[\dfrac{\ln\psi/\psi_{mMac}}{\sqrt{2}\,\sigma_{\mathrm{Mac}}}\right]\right] \\
\dfrac{\partial K_{\mathrm{Mat}}}{\partial\psi} = \dfrac{-K_s}{\sqrt{2\pi}\sigma\psi}\dfrac{\theta_{sMacMat} - \theta_r}{\theta_s - \theta_r}\mathrm{erfc}\left[\dfrac{\ln\psi/\psi_m}{\sqrt{2}\,\sigma} + \dfrac{\sigma}{\sqrt{2}}\right]\sqrt{S_e(\psi)}\exp\left[-\left[\dfrac{\ln\psi/\psi_m}{\sqrt{2}\,\sigma} + \dfrac{\sigma}{\sqrt{2}}\right]^2\right] - \\
-\dfrac{K_s}{8\sqrt{\pi}\psi}\dfrac{\theta_{sMacMat} - \theta_r}{\theta_s - \theta_r}\dfrac{\left[\mathrm{erfc}\left[\dfrac{\ln\psi/\psi_m}{\sqrt{2}\,\sigma} + \dfrac{\sigma}{\sqrt{2}}\right]\right]^2}{\sqrt{S_e(\psi)}}\left[\dfrac{\theta_{sMacMat} - \theta_r}{\theta_s - \theta_r}\dfrac{\exp\left[-\left[\dfrac{\ln\psi/\psi_m}{\sqrt{2}\,\sigma}\right]^2\right]}{\sigma} + \dfrac{\theta_s - \theta_{sMacMat}}{\theta_s - \theta_r}\dfrac{\exp\left[-\left[\dfrac{\ln\psi/\psi_{mMac}}{\sqrt{2}\,\sigma_{\mathrm{Mac}}}\right]^2\right]}{\sigma_{\mathrm{Mac}}}\right] \\
\dfrac{\partial K_{\mathrm{Mac}}}{\partial\psi} = \dfrac{-K_s}{\sqrt{2\pi}\sigma_{\mathrm{Mac}}\psi}\dfrac{\theta_s - \theta_{sMacMat}}{\theta_s - \theta_r}\mathrm{erfc}\left[\dfrac{\ln\psi/\psi_{mMac}}{\sqrt{2}\,\sigma_{\mathrm{Mac}}} + \dfrac{\sigma_{\mathrm{Mac}}}{\sqrt{2}}\right]\sqrt{S_e(\psi)}\exp\left[-\left[\dfrac{\ln\psi/\psi_{mMac}}{\sqrt{2}\,\sigma_{\mathrm{Mac}}} + \dfrac{\sigma_{\mathrm{Mac}}}{\sqrt{2}}\right]^2\right] - \\
-\dfrac{K_s}{8\sqrt{\pi}\psi}\dfrac{\theta_s - \theta_{sMacMat}}{\theta_s - \theta_r}\dfrac{\left[\mathrm{erfc}\left[\dfrac{\ln\psi/\psi_{mMac}}{\sqrt{2}\,\sigma_{\mathrm{Mac}}} + \dfrac{\sigma_{\mathrm{Mac}}}{\sqrt{2}}\right]\right]^2}{\sqrt{S_e(\psi)}}\left[\dfrac{\theta_{sMacMat} - \theta_r}{\theta_s - \theta_r}\dfrac{\exp\left[-\left[\dfrac{\ln\psi/\psi_m}{\sqrt{2}\,\sigma}\right]^2\right]}{\sigma} + \dfrac{\theta_s - \theta_{sMacMat}}{\theta_s - \theta_r}\dfrac{\exp\left[-\left[\dfrac{\ln\psi/\psi_{mMac}}{\sqrt{2}\,\sigma_{\mathrm{Mac}}}\right]^2\right]}{\sigma_{\mathrm{Mac}}}\right] \\
\textbf{elseif } \psi > 0 \\
\dfrac{\partial K}{\partial\psi} = 0
\end{cases} \tag{4}$$

2.2. Richardson–Richards' equation of HyPix model

Modelling unsaturated flow in highly heterogeneous soils can be

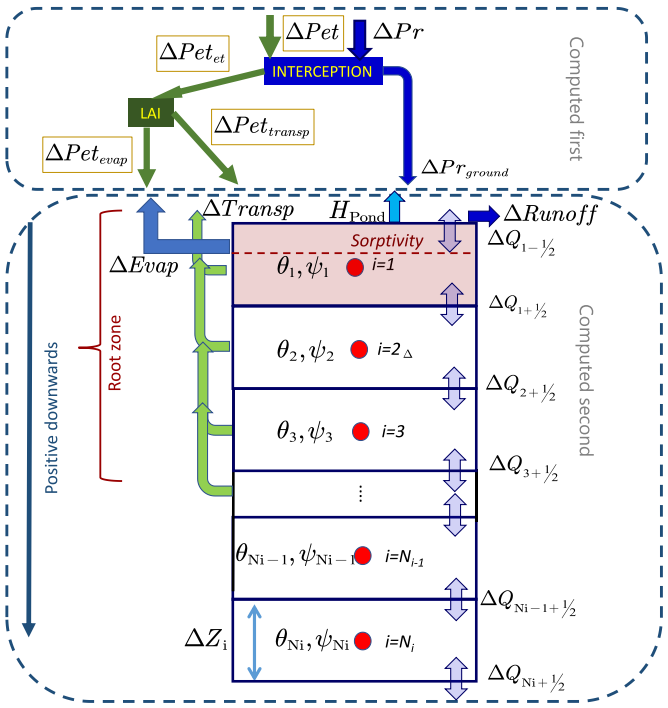

Fig. 1. Diagram describing the 1D vertical discretization of the Richardson–Richards' equation, where i is the cell number (cell 1 is the top cell and cell N_i is the bottom cell, therefore cell = i is below cell = i–1). Considering ΔX as $\sum_{t=1}^{T} X^t - \sum_{t=1}^{T-1} X^t$

then: ΔPr [L] is the precipitation reaching the top of the canopy; $\Delta Pr_{\text{ground}}$ [L] is the precipitation reaching the soil surface (cell = 1); H_{pond} [L] is the ponding water; $\Delta Runoff$ [L] is the runoff and $\Delta Q_{i+1/2} = Q_{i+1/2}\,\Delta T$ [L] is the inter-cell water volume (positive downwards). Water is removed from the soil profile by transpiration, $\Delta Transp$ [L], and evaporation, $\Delta Evap$ [L], depending on θ and potential evapotranspiration, ΔPet [L] (partitioned between potential evaporation, ΔPet_{evap} [L], and potential transpiration, $\Delta Pet_{\text{transp}}$ [L]).

accurately performed by solving the RRE (Richardson, 1922; Richards, 1931), which is commonly adopted by soil-vegetation-atmosphere transfer models (e.g., Jones et al., 2021). However, the RRE is highly non-linear, and despite numerous efforts over the last decade its solution using numerical methods is demanding, and algorithms to achieve fast and accurate solutions are still actively being researched (e.g., Zha et al., 2019). Assuming a rigid solid matrix (Fig. 1), the mixed form of the RRE is written as:

$$\frac{\theta_i(\psi_i^t) - \theta_i(\psi_i^{t-1})}{\Delta T^t} - S_o \frac{\theta_i(\psi_i^t)}{\theta_{s_i}} \frac{\psi_i^{t-1} - \psi_i^t}{\Delta T^t} = \frac{Q_{i-\frac{1}{2}}^t - Q_{i+\frac{1}{2}}^t}{\Delta Z_i} - Sink_i(\psi_i^{t-1}) \quad (5)$$

where ΔT^t [T] is the *time-step* at time t; ΔZ_i [L] is the *mesh size* of cell i, with the vertical coordinate positive downwards; θ_i [$L^3\ L^{-3}$] is the *volumetric soil water content* of cell i; θ_{s_i} [$L^3\ L^{-3}$] is the *saturated volumetric soil water content* of cell i; S_0 [L^{-1}] is a parameter which ranges from 10^{-7} to 10^{-10} that accounts for *fluid compressibility*, which is assumed to be constant with depth; ψ_i [L] is the *soil water pressure* of cell i, considering $\psi < 0$ for unsaturated soils; Q [$L\ T^{-1}$] is the *soil water flux* based on the extended DB law, which is positive downward and negative when water moves upwards; $Q_{i-\frac{1}{2}}^t$ [$L\ T^{-1}$] is the flux entering cell i and $Q_{i+\frac{1}{2}}^t$ [$L\ T^{-1}$] is the flux exiting cell i; and $Sink_i$ [$L^3\ L^{-3}\ T^{-1}$], taken as positive, is the *sink* term defined as the volume of water per unit time removed from cell i by soil *evaporation* (section 7.6.1) and *root water uptake* (section 7.6.2).

2.2.1. Water fluxes, Q

2.2.1.1. Q below the top cell: 2 ≤ i ≤ Ni. The Darcian fluid flux, $Q_{i-\frac{1}{2}}^t$ [$L\ T^{-1}$], is computed by using the inter-cell hydraulic conductivity between cell i and (i–1) as described in Fig. 1, as follows:

$$\begin{cases} Q_{i-\frac{1}{2}}^t = -K_{i-\frac{1}{2}}(\psi)\left[\dfrac{\psi_i^t - \psi_{i-1}^t}{\Delta Z_{i-\frac{1}{2}}} - \cos\alpha\right] \\ \Delta Z_{i-\frac{1}{2}} = \dfrac{\Delta Z_i + \Delta Z_{i-1}}{2} \\ K_{i-\frac{1}{2}}(\psi) = \left[w_i\left[K_i(\psi_i^t)\right]^p + [1-w_i]\left[K_{i-1}(\psi_{i-1}^t)\right]^p\right]^{1/p} \\ \omega_i = \dfrac{\Delta Z_i}{\Delta Z_i + \Delta Z_{i-1}} \end{cases} \quad (6)$$

where $Q_{i-\frac{1}{2}}^t$ [$L\ T^{-1}$] is the flux entering cell i from the top, and $Q_{i+\frac{1}{2}}^t$ is the flux exiting cell i from the bottom; $K_{i-\frac{1}{2}}$ [$L\ T^{-1}$] refers to the *weighted average* inter-cell hydraulic conductivity (e.g., Haverkamp and Vauclin, 1979; Belfort et al., 2013), computed with ω_i; $\Delta Z_{i-\frac{1}{2}}$ [L] is the distance between cell centres i and (i–1), as depicted in Fig. 1; α [radian] refers to the angle between the vertical axis and the slope of the soil's surface; and $p = 1$ for weighted average intercell conductivity as in this paper.

2.2.1.2. Top boundary conditions, i = 1: ponding and runoff. Two boundary conditions are currently available in HyPix: **(a)** novel flux boundary condition with infiltration driven by sorptivity (section 2.2.1.2.1) and **(b)** prescribed top pressure boundary condition (section 2.2.1.2.2).

2.2.1.2.1. Novel top flux boundary condition driven by sorptivity. The nomenclature taken in this paper is that ΔX is defined as $\sum_{t=1}^{T} X^t - \sum_{t=1}^{T-1} X^t$. For the top flux boundary condition, HyPix checks if the top flux boundary condition imposed by the user (throughfall precipitation $\Delta Pr_{\text{through}}^t$ [L]) can infiltrate into the top layer; if it is not the case, the excess of precipitation ponds on top of the soil surface. If ponding depth exceed the maximum ponding depth the excess water will be lost to runoff. The amount of water infiltrating into the top cell, $i = 1$, for a period ΔT, is computed by $\Delta Q_{\frac{1}{2}}^t$ [L] (Fig. 1). As the RRE cannot compute the top air–soil boundary, we compute $\Delta Q_{\frac{1}{2}}^t$ using the two-term approximation of Haverkamp et al. (1994), as suggested by Fernández-Gálvez et al. (2019). The maximum infiltration depth for a given ΔT is $\Delta Qmax_{\frac{1}{2}}^t$ [L], and is computed as:

$$\begin{cases} B = \dfrac{2-\beta}{3} + \dfrac{1+\beta}{3}\dfrac{K(\theta_1^{t-1})}{Ks_1} \\ \Delta Qmax_{\frac{1}{2}}^t = Qmax_{\frac{1}{2}}^t \Delta T^t = \left[Sorpt(\theta_1^{t-1})\sqrt{\Delta T^t} + B\,Ks_1\,\Delta T^t\right]\cos\alpha \end{cases} \quad (7)$$

where $Qmax^t_{i_{/2}}$ [L T^{-1}] is the maximum soil water flux; *Sorpt* [L $T^{-1/2}$] is the soil *sorptivity*; β [-] is an integral shape parameter, typically fixed at 0.6 (Haverkamp et al., 1994; Parlange et al., 1982); and the slope, α [radian], is the angle between the flow direction of recharge and the vertical axis ($0 \leq \alpha \leq \pi/2$ for inclined flow).

Sorptivity is computed using the mixed formulation proposed by Lassabatere et al. (2021, 2022). The novelty of this sorptivity model is that it is highly efficient and accurate in the computation of sorptivity for all soil types from oven dry to saturation. The sorptivity model is computed as:

$$\begin{cases} D(\theta) = K(\theta)\dfrac{d\psi}{d\theta} \\ Sorpt^2\left(\theta_1^{t-1}, \theta_{s_1}\right) = \displaystyle\int_{\theta_1^{t-1}}^{\frac{\theta_{s_1}-\theta_1^{t-1}}{2}} \left[\theta_{s_1} + \theta - 2\theta_1^{t-1}\right] D(\theta)d\theta + \int_{0}^{\psi\left(\frac{\theta_{s_1}-\theta_1^{t-1}}{2}\right)} \left[\theta_{s_1} + \theta(\psi) - 2\theta_1^{t-1}\right] K(\psi)d\psi \end{cases} \tag{8}$$

where $D(\theta)$ is the diffusivity function for which $d\psi/d\theta$ is derived in Eq. (3). Eq. (8) splits the integral into two parts to allow the integration of continuous functions over closed intervals. In the regular expression, the $D(\theta)$ is infinite close to saturation, $\theta \to \theta_s$. In the specific Eq. (8), the last part of the integration based on ψ is replaced with the integration of the hydraulic conductivity as a function of the water pressure, $K(\psi)$, alleviating the problem of convergence.

The maximum water infiltrating into the top cell, $\Delta Qmax^t_{i_{/2}}$, must be less than the maximum available pore volume of the top cell:

$$\begin{cases} \Delta Sink_1\left(\psi_1^{t-1}\right) = \Delta Z_i \Delta T^t Sink_1\left(\psi_1^{t-1}\right) \\ \Delta Qmax^t_{i_{/2}} = \min\left\{\Delta Qmax^t_{i_{/2}}\ ;\ \Delta Z_1\left[\theta_{s1} - \theta_1^{t-1}\right] + \Delta Sink_1\left(\psi_1^{t-1}\right)\right\} \end{cases} \tag{9}$$

where θ_{s1} [$L^3\,L^{-3}$] is the *saturated volumetric soil water content* and $\Delta Sink_1$ [L] the sink term of the top cell ($i = 1$).

The amount of water that is not able to infiltrate into the soil can either run off laterally due to the slope or get ponded at the surface, where ponding H^t_{pond}, [L] is computed as:

$$H^t_{\text{pond}} = \max\left\{\Delta Pr^t_{\text{through}} + H^{t-1}_{\text{pond}} - \Delta Qmax^t_{i_{/2}}\ ;\ 0\right\} \tag{10}$$

where $\Delta Pr^t_{\text{through}}$ [L] is the *throughfall precipitation* (i.e., the amount of water reaching the top cell; Appendix 7.5).

It is to be noted that the novel top flux boundary condition driven by sorptivity does not require any additional HyPix parameters.

Runoff, $\Delta Runoff^t$ [L], is generated if H^t_{pond} exceeds a user defined maximum ponding depth $H_{\text{pond\_max}}$[L] as follow:

$$\begin{cases} \Delta Runoff^t = \max\left\{H^t_{\text{pond}} - H_{\text{pond\_max}}\cos\alpha\ ;\ 0\right\} \\ H^t_{\text{pond}} = \min\left\{H^t_{\text{pond}}\ ;\ H_{\text{pond\_max}}\cos\alpha\right\} \end{cases} \tag{11}$$

2.2.1.2.2. Prescribed top pressure boundary condition, ψ_{top}. The prescribed top water pressure boundary condition implies that $\psi^t_1 = \psi^t_{\text{top}}$. The flux at the surface boundary is computed as follows:

$$Q^t_{i_{/2}} = -K_1\left(\psi^t_1\right)\left[\frac{\psi_1^{t-1} - \psi^t_{\text{top}}}{\Delta Z_{i/2}} - \cos\alpha\right] \tag{12}$$

where ψ^t_{top} [L] is a user-defined pressure.

HyPix computes equivalent $\Delta Pr^t_{\text{through}}$ corresponding to $\psi^t_{\text{top}} \simeq \psi_1^{t-1}$. In future research, the top water pressure boundary condition can be used to fine-tune the sorptivity model [Eq. (8)] described above.

2.2.1.3. Bottom boundary conditions, $i = N_i$. The bottom boundary conditions implemented in HyPix are special cases of the following Eq. (13) derived from Eq. (6), and include **(a)** free drainage (section 2.2.1.3.1), **(b)** prescribed bottom pressure (section 2.2.1.3.2), and **(c)** prescribed bottom flux (section 2.2.1.3.3). The bottom boundary condition is universally computed as follows:

$$Q^t_{N+i_{/2}} = -K_N\left(\psi^t_N\right)\left[\frac{\psi^t_{N+1} - \psi^t_N}{\Delta Z_{N/2}} - \cos\alpha\right] \tag{13}$$

2.2.1.3.1. Free drainage. The free drainage boundary condition at the bottom of the soil profile occurs when $\frac{\partial\psi^t_N}{\partial Z_N} = 1$ in Eq. (13), leading to:

$$Q^t_{N+i_{/2}} = K_N\left(\psi^t_N\right)\cos\alpha \tag{14}$$

2.2.1.3.2. Prescribed bottom pressure, ψ_{bot}. The prescribed bottom water pressure boundary condition, ψ^t_{bot} [L], is a user-defined variable (positive for saturated and negative for unsaturated conditions) set at the bottom of cell *N* of the soil profile (ψ^t_{N+1}), which is derived from Eq. (13) and results in the following flux:

$$Q^t_{N+i_{/2}} = -K_N\left(\psi^t_{\text{bot}}\right)\left[\frac{\psi^t_{\text{bot}} - \psi^t_N}{\Delta Z_{N/2}} - \cos\alpha\right] \tag{15}$$

2.2.1.3.3. Prescribed bottom flux, Q_{bot}. The prescribed bottom flux boundary condition, Q^t_{bot} [L], is a user-defined variable (positive as a sink and negative as a source) set at the bottom of cell *N* of the soil profile, which derived from Eq. (13) results in the following flux:

$$Q^t_{N+i_{/2}} = Q^t_{\text{bot}} \tag{16}$$

2.3. Solving the Richardson–Richards' equation using the Newton–Raphson method

The Picard and Newton–Raphson (NR) iterative methods are the most widely used procedures for solving the RRE. The NR method has been found to be more efficient than the Picard iteration method (Lehmann and Ackerer, 1998; Paniconi and Putti, 1994), so we solved the RRE using the NR algorithm. The NR method is used to solve ψ^t_i such that

the residuals of each cell, R_i^t [L], equal close to 0. R_i^t is derived from Eq. (5) as follow:

$$\begin{cases} R_i^t = \Delta Z_i\left[\theta_i\left(\psi_i^t\right) - \theta_i\left(\psi_i^{t-1}\right)\right] + \Delta Z_i S_o \dfrac{\theta_i\left(\psi_i^t\right)}{\theta_{s_i}}\left[\psi_i^t - \psi_i^{t-1}\right] - \Delta T^t\left[Q_{i-\frac{1}{2}}^t - Q_{i+\frac{1}{2}}^t\right] + \Delta Sink_i\left(\psi_i^{t-1}\right) \\ \Delta Sink_i\left(\psi_i^{t-1}\right) = \Delta Z_i \Delta T^t Sink_i\left(\psi_i^{t-1}\right) \end{cases} \tag{17}$$

where $\Delta Sink_i$ [L] is the sink computed for a given ΔT. To stabilize the numerical scheme, $\Delta Sink_i$ is computed with the ψ_i values derived from the previous time-step.

The NR method is computed using a first-order Taylor development by solving the Jacobian matrices of the residuals, R [Eq. (17)] in an iterative way that updates $[\psi_i^{t,k+1} - \psi_i^{t,k}]$ until convergence is achieved. The numerical discretization is a tridiagonal (Appendix 7.1), non-linear set of equations that needs to be solved for $[\psi_i^{t,k+1} - \psi_i^{t,k}]$, and for every iteration, k as follows:

$$\begin{cases} \psi_i^{t,k=1} = \psi_i^{t-1} \\ -R_i\left(\psi_i^{t,k}\right) = \sum_{j=i-1}^{i+1} \dfrac{\partial R_i\left(\psi_j^{t,k}\right)}{\partial \psi_j^{t,k}}\left(\psi_j^{t,k+1} - \psi_j^{t,k}\right) \end{cases} \tag{18}$$

where the derivatives are described in Appendices 7.2 and 7.3. The initial $\psi_i^{t=0}$ is derived either from measured $\theta^{t=0}$ or from $\psi^{t=0}$.

The computation of $\psi_{\min}$ [L], which is the minimum allowed value of ψ, is based on the assumption that $\theta(\psi)$ is log-normal distribution, and therefore, according to Fernández-Gálvez et al. (2021), $\psi_{\min}$ can be computed as follows:

$$\begin{cases} \psi_i^t \geqslant \psi_{\min_i} = -e^{\ln\psi_{m_i} + 4\sigma_i} \\ K(\psi_{\min_i}) \approx 0 \end{cases} \tag{19}$$

The computation of $\psi_{\max}$ [L], which is the maximum allowed value of ψ, is more challenging to compute as it can be positive or negative. Therefore, during the iteration when the water pressure is close to saturation it may change sign causing numerical instability (Zha et al., 2017). To increase numerical stability for soils close to saturation, $\psi_{\max}$ switches depending on the value of ψ_i^{t-1} as follow:

$$\begin{cases} \textbf{if } \psi_i^{t-1} > -\dfrac{\psi_{\text{MacMat}}}{2} \\ \psi_{\max_i}^t = \psi_{\text{maxMax}} \\ \textbf{elseif} \\ \psi_{\max_i}^t = 0 \end{cases} \tag{20}$$

where ψ_{MacMat} [L] is the theoretical water pressure for which macropore starts to fill up, corresponding to the minimum water pressure for which a soil can be considered close to saturation, often taken as 100 mm (e.g., Jarvis, 2007); ψ_{maxMax} is a parameter for which its feasible range is provided in Table 1.

Table 1 shows the feasible range as well as the recommended values for the parameters required to solve the RRE with the HyPix model.

2.3.1. Convergence criterion

For a given time-step, the iteration of the NR method stops either when $k = N_k$, where N_k is a user-defined maximum number of iterations (Table 1), or when the overall water balance of the residuals, WB_{residual} [T^{-1}], is satisfied. The WB_{residual} convergence criterion for the NR method is based on the Euclidean norm of a vector R (e.g., Driscoll and Braun, 2017; Kochenderfer and Wheeler, 2019; Kelley, 2003):

$$WB_{\text{residual}} \geqslant \sqrt{\frac{\sum_{i=1}^{N_i}\left[\frac{R_i^t}{\Delta T^t \Delta Z_i}\right]^2}{N_i}} \tag{21}$$

where N_i is the total number of cells, as described in Fig. 1. The residuals are normalized, such that WB_{residual} is independent of the *cell size*, ΔZ, and the *time-step*, ΔT^t. The feasible range of WB_{residual} is provided in Table 1.

2.3.2. Automatic differentiation of the Jacobian with Julia language

One of the shortcomings of the NR solver is that it requires the mathematical derivatives of R (Eq. (18) and derivatives described in Appendices 7.2 and 7.3), the implementation of which can be complicated and time consuming (e.g., modifying the inter-cell hydraulic conductivity [Eq. (6)] for testing purposes, requires recalculation of the derivatives).

To address this shortcoming, HyPix implements an option whereby the derivatives are derived automatically by using the forward-mode automatic differentiation *ForwardDiff* in the Julia package (Revels et al., 2016) (https://github.com/JuliaDiff). *ForwardDiff* (version 0.10.24) was found to be as accurate as using the mathematical derivatives and only, on average, 16% slower compared with using the analytical derivatives. We tested that for every boundary condition (section 2.2.1.2 and section 2.2.1.3), the derivatives derived analytically (section 7.2) give the same results (accuracy 10^{-8}) to those derived by using the forward-mode automatic differentiation *ForwardDiff*.

2.3.3. Adaptive time-stepping management

The time-stepping management module optimizes the size of the time-step, ΔT, such that HyPix uses the largest ΔT while meeting the targeted water balance and accuracy of the solution. Among the heuristic time-stepping methods in the literature, we selected and improved the adaptive time-stepping management of Kirkland et al. (1992) and Ross (2003). This method is physically based, such that ΔT is directly derived from the residuals of the water balance (Eq. (17)) and requires

Table 1
Minimum, maximum, and recommended values for the HyPix parameters required to solve the RRE.

	$\Delta\psi_{\text{active}}$ [mm] Eq. (22)	$\Delta T_{\min}$ [s] Eq. (22)	$\Delta T_{\max}$ [s] Eq. (22)	N_k [-] Section 2.3.1	WB_{residual} [s^{-1}] Eq. (21)	$\Delta\theta_{\max}$ [$L^3\,L^{-3}$] Eq. (22)	$\Omega_{\min}$ [-] Eq. (31)	ψ_{maxMax} [mm] Eq. (20)
Min	0.5	1	ΔT_{min}	10	10^{-8}	10^{-2}	0.1	10^4
Max	10	$\Delta T_{\max}$	6000	100	10^{-20}	10^{-6}	0.5	10^6
Recom.	1.0	30	5400	70	10^{-10}	8.10^{-3}	0.2	10^5

only one physical parameter. ΔT is calculated via a maximum increase or decrease of the degree of saturation for each cell. This ensures a higher time resolution when θ variations are large, which improves the convergence rate at the wetting front.

Below we present three options to optimize the size of the time-step: **(a)** the traditional time-stepping management of Kirkland et al. (1992) and Ross (2003), developed specifically for the RRE and based on θ with a more realistic computation of average ΔT^t (section 2.3.3.1), **(b)** a novel time-stepping management of Kirkland et al. (1992) and Ross (2003), adapted for RRE based on ψ and implemented in HyPix (section 2.3.3.2), and **(c)** a condition to rerun HyPix with the updated ψ and ΔT^t (section 2.3.3.3).

2.3.3.1. Traditional adaptive time-stepping management: Time-stepping-$\Delta\theta$. The time-stepping management of Kirkland et al. (1992) and Ross (2003) assures numerical stability and avoids oscillation in the solution. ΔT is derived by rearranging the terms of the residual (Eq. (17)) assuming that $R \approx 0$ and $S_0 \approx 0$ (S_0 is by definition small and strictly 0 for non-compressible fluids) and $\Delta\theta_{\max} \approx \left|\theta_i(\psi_i^t) - \theta_i(\psi_i^{t-1})\right|$ where $\Delta\theta_{\max}$ [L^3 L^{-3}] is a constant parameter describing the maximum change of θ for a given ΔT. The $\Delta\theta_{\max}$ feasible range is provided in Table 1.

We improved the time-stepping computing ΔT^t by putting more weight on cells that are dynamically active $Q^t_{i-1/2} \neq Q^t_{i+1/2}$ with $\left|\psi_i^t - \psi_{i-1}^t\right| \geqslant \Delta\psi_{\text{active}}$. In other words, HyPix computes ΔT^t considering the cells that are wetting up due to, for example, a wetting front in an initially dry soil (bottom cells are inactive). Therefore ΔT^t is computed as follows:

$$\begin{cases} N_{iT} = 1 \\ \textbf{for } i = 1 : N_i \\ \textbf{if } \left|\psi_i^t - \psi_{i-1}^t\right| \geqslant \Delta\psi_{\text{active}} \\ \Delta T_i^t = \dfrac{\Delta Z_i \Delta\theta_{\max} + \Delta Sink_i\left(\psi_i^{t-1}\right)}{\left|Q^t_{i-1/2}\left(\psi_{i-1}^{t-1}\right) - Q^t_{i+1/2}\left(\psi_i^{t-1}\right)\right|} \\ \Delta T_{\min} \leqslant \Delta T_i^t \leqslant \Delta T_{\max} \\ N_{iT} = N_{iT} + 1 \\ \textbf{end} \\ \textbf{end} \\ \Delta T^t = \sqrt{\dfrac{\sum_{i=1}^{N_i}\left[\Delta T_i^t\right]^2}{N_{iT}}} \end{cases} \tag{22}$$

where $\Delta T_{\min}$ [T] and $\Delta T_{\max}$ [T] are user-defined minimum and maximum time-steps, described in Table 1, which are used for 'safety' in the code; $\Delta\psi_{\text{active}}$ with a recommended constant value of 1.0 mm, also described in Table 1; and N_i is the total number of cells.

The selected average ΔT^t of a soil profile is computed from ΔT_i^t which is derived from every cell using a modified Euclidean norm of a vector based on Driscoll and Braun (2017), Kochenderfer and Wheeler (2019), and Kelley (2003), as computed for WB_{residual} in section 2.3.1.

As described in Eq. (22), the computational time in HyPix decreases as ΔT increases. ΔT increases when **(a)** the size of the cell, ΔZ, increases, **(b)** the hydraulic properties from one cell to another, depicted by Q, do not change dramatically, **(c)** there are small pressure gradients, $\partial\psi/\partial Z$, **(d)** there are small differences in hydraulic properties, and **(e)** when $\Delta\theta_{\max}$ increases.

2.3.3.2. Novel adaptive time-stepping management: Time-stepping-ψ. For the robustness of the solution of the RRE [Eq. (5)] based on ψ, changes of $\Delta\psi$ between two consecutive time-steps must be small. This is particularly the case when simulating infiltration into dry soil, where the head gradient at the wetting front is extremely large, leading to large computational efforts, numerical instability, and inaccuracy (e.g., Zha et al., 2017). Nevertheless, describing a generic $\theta(\psi)$, a small change of $\Delta\theta$ could result in a large change in $\Delta\ln\psi$, particularly near saturation and at the dry end of the $\theta(\psi)$ curve.

The traditional Ross (2003) time-stepping-$\Delta\theta$ (Eq. (22)) is modified by allowing $\Delta\theta_{\max}$ to vary as described by $\Delta\theta^t_{\max_i}(\psi)$ such that $\Delta\ln\psi$ = const. For this we introduce a temporary parameter, computed from and for every cell:

$$\Delta\ln\psi_{\max_i} \geqslant \left|\ln\left(1+\psi_i^t\right) - \ln\left(1+\psi_i^{t-1}\right)\right| \tag{23}$$

To avoid introducing a second parameter we derive $\Delta\ln\psi_{\max}$ from $\Delta\theta_{\max}$. For a given $\psi(\theta)$, the smallest $\Delta\ln\psi$ occurs at $(\theta_r + \theta_{sMacMat})/2$ (or at the Kosugi parameter $\psi = \psi_m$). Therefore, $\Delta\ln\psi_{\max_i}(\Delta\theta_{\max})$ is computed for every cell as follows:

$$\begin{cases} \theta_{1/2\,i} = \dfrac{\theta_{r_i} + \theta_{sMacMat_i}}{2} = \theta(\psi_m) \\ \Delta\ln\psi_{\max_i}(\Delta\theta_{\max}) = \dfrac{\ln\left[\psi\left(\theta_{1/2\,i} - \dfrac{\Delta\theta_{\max}}{2}\right) + 1\right] - \ln\left[\psi\left(\theta_{1/2\,i} + \dfrac{\Delta\theta_{\max}}{2}\right) + 1\right]}{2} \end{cases} \tag{24}$$

$\Delta\theta^t_{\max_i}(\psi)$ is adjusted based on the maximum allowed change of $\Delta\ln\psi_{\max_i}$ and ψ_i^t:

$$\Delta\theta^t_{\max_i}\left(\psi_i^t,\ \Delta\psi_{\max_i}\right) = \theta_i e^{\ln\left(\psi_i^t+1\right)}\left(e^{-\Delta\ln\psi_{\max_i}} - e^{\Delta\ln\psi_{\max_i}}\right) \tag{25}$$

The advantage of $\Delta\theta^t_{\max_i}(\psi) \leqslant \Delta\theta_{\max}$ is that its 'steps' are smaller at the wet end of the $\theta(\psi)$ curve. ΔT_i^t is computed by substituting $\Delta\theta^t_{\max_i}(\psi)$ instead of $\Delta\theta_{\max}$ into Eq. (22).

2.3.3.3. Condition to rerun the time-step. ΔT^t is computed using the previous water pressure, ψ^{t-1}, which may not reflect, for example, the passage of a wetting front requiring a reduced ΔT^t. Therefore, to assure accurate water balance and stability of the solution of the RRE, HyPix is rerun with the updated ΔT^t if $\Delta T^t(\psi^t) \ll \Delta T^t(\psi^{t-1})$. Therefore, HyPix is rerun if the following condition is meet:

$$\Delta T^t\left(\psi^{t-1}\right) < \frac{\Delta T_{\min} + P_{\Delta T\_\text{Rerun}}}{2} \tag{26}$$

where $\Delta T_{\min}$ is the minimum time-step described in Table 1.

If the maximum number of iterations is reached, $k = N_k$ and the condition Eq. (26) is not met, then HyPix is rerun with a reduced time-step as follows:

$$\Delta T^t = \frac{\Delta T_{\min} + P_{\Delta T\_\text{Rerun}}}{2} \tag{27}$$

2.3.4. Controlling Newton–Raphson step

The following algorithms are strategies to control the size of the NR step, defined as:

$$\Delta NRstep_i = \left|\psi_i^{t,k} - \psi_i^{t,k-1}\right| \tag{28}$$

NR steps are implemented to avoid numerical instability and 'overshooting' of the NR method. The following algorithms are implemented into HyPix: **(a)** absolute convergence criterion (section 2.3.4.1); **(b)**

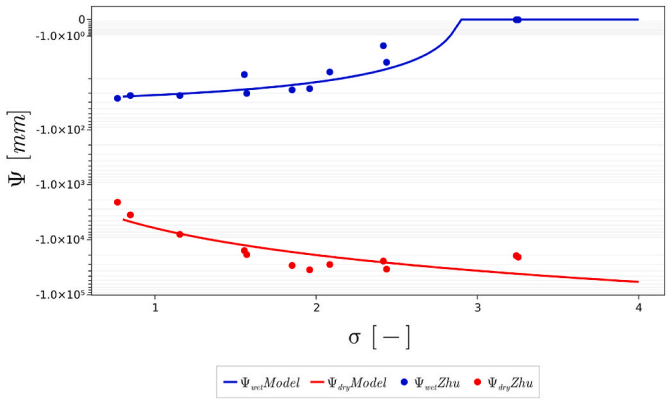

Fig. 2. ψ_{dry} and ψ_{wet} model as a function of σ derived for the set of soils used in Zha et al. (2017).

traditional smoothing method (section 2.3.4.2); **(c)** novel dynamic smoothing method (section 2.3.4.3); and **(d)** modified iteration for initially dry conditions proposed by Zha et al. (2017) (section 2.3.4.4). The advantages of the different algorithms as well as the rationality of the recommended option in HyPix are presented in the discussion.

2.3.4.1. Absolute convergence criterion: *traditional absolute convergence criterion to avoid overshooting of the NR step.* In line with common practices of solving the RRE, the *absolute convergence criterion* constrains the NR step by using $\Delta\ln\psi_{\max_i}$ [Eq. (24)]. In HyPix for every cell $\Delta NRstep_i$ [Eq. (28)] is constrained as follows:

$$e^{\Delta\ln\psi_{\max}} + 1 \geqslant \max\left\{\left|\psi_i^{t,k} - \psi_i^{t,k-1}\right|_{i=1}^{i=N_i}\right\} \tag{29}$$

This absolute convergence criterion could be used in conjunction with other constraining methods described in the following sections.

2.3.4.2. Constant Ω: *traditional smoothing with constant Ω to avoid overshooting of the NR step.* To reduce overshooting of the NR step between two iterations and increase the efficiency, we introduce a smoothening algorithm as follows:

$$\psi_i^{t,k+1} = \Omega\psi_i^{t,k+1} + [1-\Omega]\psi_i^{t,k} \tag{30}$$

were $\Omega = 0.5$ is a fixed parameter.

2.3.4.3. Dynamic Ω: *novel smoothing with dynamic Ω to avoid overshooting of the NR step.* The introduction of Ω, such as constant Ω in section 2.3.4.2, was found to be highly successful in reducing convergence failure. We therefore propose to improve the method such that Ω varies for every cell and iteration. The feasible range of Ω is $[\Omega_{\min}, \Omega_{\max}]$ where $\Omega = \Omega_{\max} = 1$ means no reduction of the NR step and $\Omega = \Omega_{\min} >$ 0 corresponds to a maximum reduction in the NR step. A decrease of Ω causes a slower convergence rate but increases the success rate of convergence of the NR for challenging conditions. We therefore propose the following Ω algorithm:

$$\begin{cases} \Omega_i^{t,k+1}\left(\psi_i^{t,k}\right) = \Omega_{\max} - [\Omega_{\max} - \Omega_{\min}]\left[\min\left\{\dfrac{\left|\theta\left(\psi_i^{t,k+1}\right) - \theta\left(\psi_i^{t,k}\right)\right|}{\Delta\theta_{\max_i}^t\left(\psi_i^{t,k+1}\right)};\ 1\right\}\right]^2 \\ \psi_i^{t,k+1} = \Omega_i^{t,k+1}\left(\psi_i^{t,k}\right)\psi_i^{t,k+1,a} + \left[1 - \Omega_i^{t,k+1}\left(\psi_i^{t,k}\right)\right]\psi_i^{t,k} \end{cases} \tag{31}$$

where $\Delta\theta_{\max_i}^t(\psi_i^{t,k+1})$ was derived from Eq. (25); $\Omega_{\max} = 1$; and the feasible range of $\Omega_{\min}$ is provided in Table 1.

At a given t, challenging situations for iteration k occur when $\left|\theta(\psi_i^{t,k+1}) - \theta(\psi_i^{t,k})\right| \ll \Delta\theta_{\max_i}^t(\psi_i^{t,k+1})$, then the NR step is reduced. It will be shown that the dynamic Ω method is not only successful in increasing accuracy but also in increasing the speed of convergence.

2.3.4.4. Dry method: *modified iteration for initially dry conditions.* Convergence failure normally occurs in some unfavourable flow conditions, especially when simulating infiltration into initially dry soils. To overcome this numerical difficulty, we adopt the algorithm proposed by Zha et al. (2017) where the water pressure before ($\psi_i^{t,k}$) and after ($\psi_i^{t,k+1}$) the iteration is examined to determine if there is any oscillation at the dry end of the $\theta(\psi)$ curve. If $\psi_i^{t,k}$ is smaller than a user-specified threshold ψ_{dry}, and $\psi_i^{t,k+1}$ is greater than a user-specified threshold ψ_{wet}, the risk of numerical divergence for this node is deemed to be very high. Under this condition, $\psi_i^{t,k+1}$ is estimated from the derived $\theta_i^{t,k+1}$ (the soil water capacity of the Bimodal Kosugi model Eq. (3)):

$$\begin{cases} \textbf{if } \psi_i^{t,k} \leqslant \psi_{dry}(\sigma_i) \textbf{ and } \psi_i^{t,k+1} \geqslant \psi_{wet}(\sigma_i) \\ \psi_i^{t,k+1} = \psi\left(\theta_i^{t,k+1}\right) = \psi\left(\theta_i^{t,k} + \dfrac{\partial\theta_i^{t,k}}{\partial\psi_i^{t,k}}\left[\psi_i^{t,k+1} - \psi_i^{t,k}\right]\right) \end{cases} \tag{32}$$

The threshold values ψ_{dry} and ψ_{wet} depend on soil type, and because σ defines the slope of the $\theta(\psi)$ curve, we derived the following empirical expressions as a function of σ with the set of soils published by Zha et al. (2017) and shown in Fig. 2.

$$\begin{cases} \psi_{wet_i} = -\max\left\{-2.312\sigma_i^2 - 2.937\sigma_i + 27.830\ ;\ 0\right\} \\ \psi_{dry_i} = -\exp[1.622\ \ln\sigma_i + 8.727] \end{cases} \tag{33}$$

2.4. Accuracy and efficiency of simulations

2.4.1. Water balance

The overall water balance, *WB* [L], of the simulation is derived from the residuals, *R* [Eq. (17)], and is computed for every time-step as follows:

Table 2
Length of soil profile (L [mm]), total time of simulation (ΣT [days]), initial conditions (IC [mm]), boundary conditions at the surface (BC_{top} for prescribed ψ [mm] or prescribed flux $Q_{1/2}^t$ $Q_{1/2}^t$ [mm s^{-1}]), boundary condition at the bottom (BC_{bot} for prescribed ψ [mm], prescribed flux $Q_{N+\,1/2}^t$ [mm s^{-1}] or free drainage). The residual and saturated water contents (θ_r and θ_s), Kosugi shape parameters (ψ_m and σ), and saturated hydraulic conductivity (K_s) for the five different test cases.

	L [mm]	ΣT [days]	IC [mm]	BC_{top}	BC_{bot}	θ_r [m^3 m^{-3}]	θ_s [m^3 m^{-3}]	ψ_m [mm]	σ [-]	K_s [mm s^{-1}]
TC1	1000	2	10^4	$\psi = 750$	$\psi = 10^4$	0.097	0.368	602.64	1.137	0.09220
TC2	1000	2	10^4	$\psi = 750$	Free	0.097	0.368	602.64	1.137	0.09220
TC3	2000	30	Z-2000	$Q_{1/2}^t = 3.75{\cdot}10^{-5}$	$\psi = 0$	0.122	0.410	5201.72	2.085	0.00072
TC4	600	30	1000	$Q_{1/2}^t = 2.3{\cdot}10^{-4}$	Free	0.024	0.366	588.42	0.981	0.06260
	600		1000			0.141	0.469	4524.09	1.933	0.00151
	600		1000			0.024	0.366	588.42	0.981	0.06260
TC5	600	16	1000	$Q_{1/2}^t = 2.3{\cdot}10^{-4}$	$Q_{N+\,1/2}^t = 0$	0.024	0.366	588.42	0.981	0.06260
	600		1000			0.141	0.469	4524.09	1.933	0.00151
	600		1000			0.024	0.366	588.42	0.981	0.06260

Table 3
For each of the test cases using the HYDRUS and HyPix models, *WB* [Eq. (35)] is the overall water balance and E_{ff} [Eq. (36)] is the average number of iterations per day homogenised for an average period of 30 days. $\Delta Q^{N_{it}}_{N+1/2} = \Delta T^{N_{it}} Q^{N_{it}}_{N+1/2}$ is the drainage from the bottom cell during the total time of simulation. *RMSE* [Eq. (37)] and *NSE* [Eq. (38)] refer to the root mean square error and Nash–Sutcliffe efficiency coefficient, respectively, computed for simulated θ-profile derived with HYDRUS and HyPix models. HyPix simulations were derived using the dynamic Ω (section 2.3.4.3), the dry method (section 2.3.4.4) for controlling the NR steps, as well as the time-stepping management based on ψ for solving the RRE (section 2.3.3.2).

	WB [mm]		E_{ff} [day^{-1}]		$\Delta Q^{N_{it}}_{N+1/2}$ [mm]		*RMSE* [mm]	*NSE* [-]
	HYDRUS	**HyPix**	**HYDRUS**	**HyPix**	**HYDRUS**	**HyPix**		
TC1	5.3 10^{-5}	1.5 10^{-5}	2374	73	15.9	13.5	4.1 10^{-3}	0.98
TC2	3.8 10^{-5}	1.1 10^{-6}	84	55	6.8	6.2	3.9 10^{-3}	0.93
TC3	2.1 10^{-4}	2.7 10^{-5}	50	34	26.7	26.7	1.0 10^{-5}	0.99
TC4	8.2 10^{-4}	2.5 10^{-5}	50	34	483	485	5.3 10^{-3}	0.99
TC5	1.4 10^{-3}	6.8 10^{-7}	61	221	5.10^{-4}	0.0	1.8 10^{-2}	0.97

Table 4
Yearly average values of precipitation (ΔPr), potential evapotranspiration (ΔPet), simulated throughfall precipitation ($\Delta Pr_{\text{through}}$), simulated drainage ($\Delta Q$), simulated evapotranspiration ($\Delta Sink$), and computed normalized WB^{η} for the five experimental sites.

Site	ΔPr	ΔPet	$\Delta Pr_{\text{through}}$	*Interception loss*	ΔQ	$\Delta Sink$	WB^{η}
	[mm]	[mm]	[mm]	[%]	[mm]	[mm]	[%]
Waitoa	1028	910	823	20	392	388	$4.4{\cdot}10^{-6}$
Waihou	1217	761	1099	10	628	433	$0.2{\cdot}10^{-6}$
Taupō	1646	773	1489	10	1015	423	$0.7{\cdot}10^{-6}$
Otorohanga	1818	875	1581	14	1162	430	$2.4{\cdot}10^{-6}$
Hamilton	2487	413	2298	8	2020	100	$0.2{\cdot}10^{-6}$

$$WB^t = \sum_{i=1}^{N_i} \Delta Z_i \left[\theta_i\left(\psi_i^t\right) - \theta_i\left(\psi_i^{t=0}\right)\right] - \sum_{i=1}^{N_i}\sum_{t=1}^{N_t} \Delta Z_i S_o \frac{\theta_i\left(\psi_i^t\right)}{\theta_{s_i}} \left[\left|\psi_i^t\right| - \left|\psi_i^{t-1}\right|\right] - \sum_{t=1}^{N_t} \Delta T^t \left[Q^t_{1/2} - Q^t_{N+1/2}\right] + \sum_{i=1}^{N_i}\sum_{t=1}^{N_t} \Delta Sink_i\left(\psi_i^t\right) \tag{34}$$

where N_t is the final time-step and N_i is the bottom cell.

It is expected that the *WB* error increases with the length of the simulation; it is therefore normalized, WB^{η}, to the cumulative infiltration:

$$WB^{\eta} = \frac{WB^t}{\sum_{t=1}^{N_t} \Delta T^t Q^t_{1/2}} \tag{35}$$

An acceptable water balance at the end of the simulation occurs when WB^{η} is smaller than the uncertainty of measuring precipitation.

2.4.2. Efficiency

The *efficiency* of a simulation, E_{ff} [T^{-1}], is defined as the average number of iterations required to perform a day of simulation, computed as follows:

$$E_{ff} = \varsigma \frac{\sum_{t=1}^{N_t} k^t}{\sum_{t=1}^{N_t} \Delta T^t} \tag{36}$$

where k is the number of iterations per time-step, which includes repeated simulation (section 2.3.3.3); N_t is the number of time-steps; and $\varsigma = 86400$ s (if the units are in seconds). Therefore, the smaller E_{ff}, the faster HyPix would run for a given WB_{residual} [Eq. (21)].

2.5. Summary of HyPix algorithm

Initialization.

- Estimate the percentage of roots, ΔRdf_i, per cell, derived from the vegetation parameters [Eq. (80)].
- Compute initial soil water pressure, ψ_{ini} [L], if required, derived from initial observed $\theta^{t=1}$.
- Compute $\Delta\psi_{\max_i}(\Delta\theta_{\max_i})$ for every cell, which will be used to compute the variable time-step [Eq. (25)] and the dynamic Ω [Eq. (31)].

Iteration of the NR, which solves ψ of the RRE for a given ΔT.
Compute at the beginning of every time-step:

- new time-step, ΔT, derived from ψ^{t-1} (section 2.3.3.2)
- *sorptivity* from ψ^{t-1} to derive the maximum infiltration rate (section 2.2.1.2.1)
- interpolation of ΔPr and ΔPet_{evap} for a given ΔT
- vegetation parameters *LAI* and K_C, which vary monthly (section 3.2.2)
- potential evapotranspiration: $\Delta Pet_{\text{transp}}$ and ΔPet_{evap} (section 7.4)
- precipitation not intercepted that reaches the ground surface, ΔPr_{ground} (section 7.5)
- soil evaporation computed from ψ^{t-1}, $\Delta Evap$ (section 7.6.1)
- root water uptake computed from ψ^{t-1}, ΔRwu (section 7.6.2).

During each iteration:

- compute the residuals [Eq. (17)] and derivatives [Eq. (18)] described in sections 7.2 and 7.3
- compute $\Delta\theta^t_{\max_i}(\psi_i^{t,k+1})$ [Eq. (25)] to manage the NR steps
- compute dynamic $\Omega_i^{t,k+1}(\psi_i^{t,k})$ [Eq. (31)] to smoothen the Newton-Raphson step
- continue the iteration loop of the NR until either the convergence criterion WB_{residual} is met Eq. (21) or the maximum allowed iteration is reached.

After iteration is computed:

- rerun the model if $\Delta T^t(\psi^t) \ll \Delta T^t(\psi^{t-1})$ with the new derived time-step (section 2.3.3.3).

After the simulation is terminated.

- Compute the soil water balance and efficiency of simulation (section 2.4).

- Compute the outputs of interest at the time step of interest (e.g., θ, ψ, Q …).

3. Material and methods

Two independent sets of data are used in this study: **(1)** we describe five synthetic test cases for validating HyPix with HYDRUS without including the sink term in the RRE, and **(2)** we present the experimental data from five contrasting sites used for testing HyPix options under field conditions including the sink term. For all test cases considered in this work, we assumed that there is no runoff and therefore $H_{\text{pond\_max}} = +\infty$.

3.1. Synthetic test cases for validating HyPix with HYDRUS without the sink term

To assess the accuracy, efficiency, and computational costs of the different algorithms of HyPix, we compared the numerical solution of HYDRUS (version 4.17.0140) (Radcliffe and Simunek, 2010; Šimůnek et al., 2016) with HyPix by using five challenging published test cases. The algorithm of HyPix utilizes the recommended options and the recommended HyPix parameters (Table 1). The HYDRUS model utilizes the recommended parameters except for the maximum time step $\Delta T_{\max}$ being reduced to 1 h and by increasing the maximum number of iterations N_k to match that of HyPix described in Table 1.

The reported test cases in the literature use the Mualem–van Genuchten hydraulic functions (Mualem, 1976; van Genuchten, 1980), and we transformed them into the Kosugi (1994, 1996) hydraulic functions, ensuring the optimal ψ_m and σ Kosugi hydraulic parameters were physically sound by using the method described in Fernández-Gálvez et al. (2021). A description of the different test cases, which combine different soil profiles with contrasting initial and boundary conditions (**TC1** to **TC5**), are summarized below.

- **TC1:** infiltration in a homogeneous initially *dry sandy loam* soil with constant prescribed pressure at the surface and prescribed pressure at the bottom (Celia et al., 1990). This test case is challenging to converge because it models the passage of a wetting front in an initially very dry soil with sudden variation of ψ.
- **TC2:** same as TC1 but with a free drainage bottom boundary condition.
- **TC3:** infiltration in a homogeneous *clay loam soil* initially at hydrostatic equilibrium with a prescribed constant flux at the soil surface and prescribed water table at the bottom (Miller et al., 1998). The profile has linearly decreasing ψ initial conditions. This test case models slow-moving water in the presence of a water table.
- **TC4:** infiltration at a constant rate into an initially dry heterogeneous soil with constant top flux at the surface and a free drainage bottom boundary condition (Zha et al., 2017). The soil profile consists of three layers of equal thickness with a clay loam layer sandwiched between two sandy loam layers (Lehmann and Ackerer, 1998). The challenge of this test case is to model the movement of water at the interface of very contrasting soils.
- **TC5:** same as TC4 but with an impermeable bottom boundary condition (Zha et al., 2017). This test case is even more challenging than TC4 as the bottom boundary condition implies a change in the direction of the water fluxes when the wetting front reaches the impermeable bottom layer.

The soil hydraulic parameters, boundary conditions, and initial conditions for the five test cases considered are listed in Table 2 The vertical discretization, used in the simulations for the test cases, was $\Delta Z = 10$ mm.

3.1.1. Goodness of fit between HYDRUS and HyPix

The goodness of fit between the model outputs corresponding to the profile soil water content from HYDRUS and HyPix was assessed using the root mean-squared error, *RMSE*, and the Nash–Sutcliffe efficiency coefficient, *NSE*, during a particular period, as follows:

$$RMSE = \sqrt{\frac{\sum_{t=1}^{N_t}\left[\sum_{i=1}^{N_i}\left[\Delta Z_i\left[\theta^t_{i\ \text{HYDRUS}} - \theta^t_{i\ \text{HyPix}}\right]\right]\right]^2}{N_t}} \tag{37}$$

$$NSE = \max\left\{1 - \frac{\sum_{t=1}^{N_t}\sum_{i=1}^{N_i}\left[\Delta Z_i\left[\theta^t_{i\ \text{HYDRUS}} - \theta^t_{i\ \text{HyPix}}\right]\right]^2}{\sum_{t=1}^{N_t}\left[\sum_{i=1}^{N_i}\Delta Z_i\theta^t_{i\ \text{HYDRUS}} - \overline{\Delta Z_i\theta^t_{i\ \text{HYDRUS}}}\right]^2}\ ;\ 0\right\} \tag{38}$$

where $\theta^t_{i\ \text{HYDRUS}}$ and $\theta^t_{i\ \text{HyPix}}$ refer to simulated soil water content values at each cell computed with HYDRUS and HyPix, respectively, for which both models utilize the same vertical discretization ($\Delta Z_i = 10$ mm). Note that $\overline{\Delta Z_i\theta^t_{i\ \text{HYDRUS}}}$ is the mean value for every cell i.

3.2. Field experimental data for testing HyPix options with sink term

3.2.1. Soils description

The five sites used in this study are dairy-cattle-grazed pasture located in the Waikato region of New Zealand. All soils have formed from airfall volcanic tephra, but vary in their soil physical properties and heterogeneity, particularly their texture and profile drainage characteristics. A brief description of the soils follows.

The ***Taupō*** soil is a sandy-textured soil formed from volcanic airfall pumice material (New Zealand classification: *Podzolic Orthic Pumice soil;* USDA Soil Taxonomy classification: Orthod (Hewitt, 2010). The ***Otorohanga*** and ***Waihou*** soils are also formed from airfall volcanic material, but with finer tephra material compared with the ***Taupō***, resulting in silty loam topsoil textures grading to silty clay in the subsoil. They are classified in New Zealand as Typic Orthic Allophanic Soils, and in Soil Taxonomy as a Haplohumult (Hewitt, 2010). Based on the soil morphology, the ***Otorohanga*** and ***Waihou*** soils would be considered to have the least heterogeneous soil profiles of those used in this study since they have a reduced number of distinct layers. The ***Taupō*** site is expected to show more heterogeneity in water movement due to the stone content (Cichota et al., 2016). The ***Hamilton*** soil has a silt loam topsoil overlying clayey, textured subsoils, having formed into strongly weathered volcanic tephra. It is classified in New Zealand as a Typic Orthic Granular Soil, and in Soil Taxonomy as a Haplohumult (Hewitt, 2010). The ***Waitoa*** soil is a silty-textured soil. It is classified in New Zealand as a Typic Orthic Gley Soil, and in Soil Taxonomy as a Haplohumult (Hewitt, 2010). The soil morphology of ***Hamilton*** and ***Waitoa*** shows the greatest heterogeneity of the soils in this study, as reflected in previous studies of soils with impeded drainage features (McLeod et al., 2008; Vogeler et al., 2019).

3.2.2. Vegetation data

Experimental sites are five mixed, non-irrigated pasture grass sites. The trapezoidal (Feddes et al., 1978) water stress response function (section 7.6.2) was used with parameters for mixed pasture grass in New Zealand derived from Wesseling (1991). For all sites, we used default values at four soil water pressures: $\psi_{\text{Feddes1}} = -100$ mm, $\psi_{\text{Feddes2}} = -250$ mm, $\psi_{\text{Feddes3}} = -5000$ mm, and $\psi_{\text{Feddes4}} = -80{,}000$ mm, and the maximum root depth, Z_{Nroot}, was averaged to 800 mm (Vogeler and Cichota, 2019) and percentage of roots in the top 300 mm, ΔRdf_{top}, was 90% (Evans, 1978). The crop coefficient, K_C, and the *LAI* (section 7.6.2) vary throughout the growing season. The range of K_C, 0.8 to 0.95 was taken from rotated grazing pasture according to an FAO irrigation paper 56 (Allen et al., 1998) and the range of the *LAI*, 0.19 to 5.10 was taken from Van Housen (2015).

3.2.3. Climate and soil water content data

Daily values of *precipitation*, ΔPr [L], were measured using a tipping

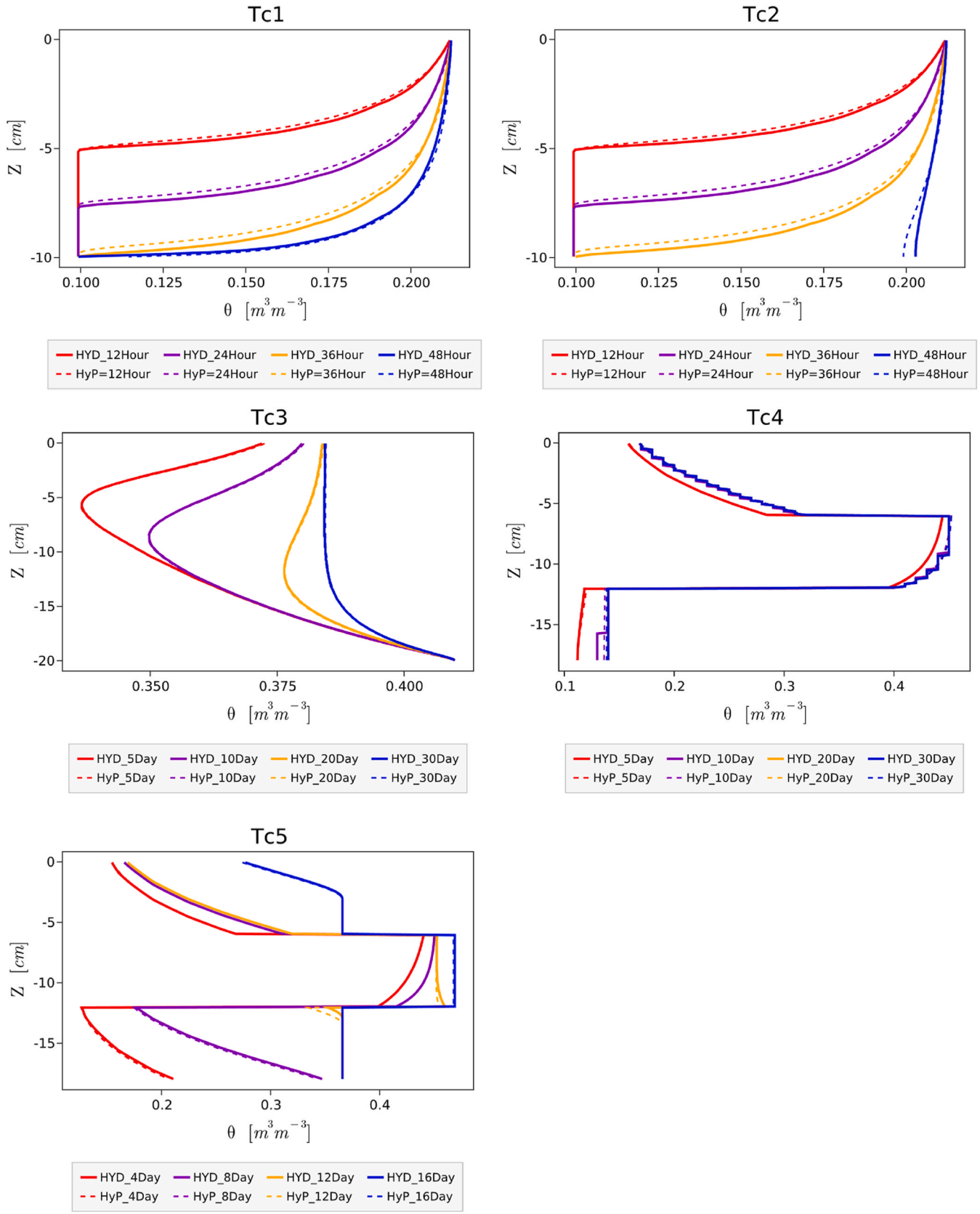

Fig. 3. Simulated θ-profile at selected periods using HYDRUS and HyPix models for the different test cases described in section 3.1.

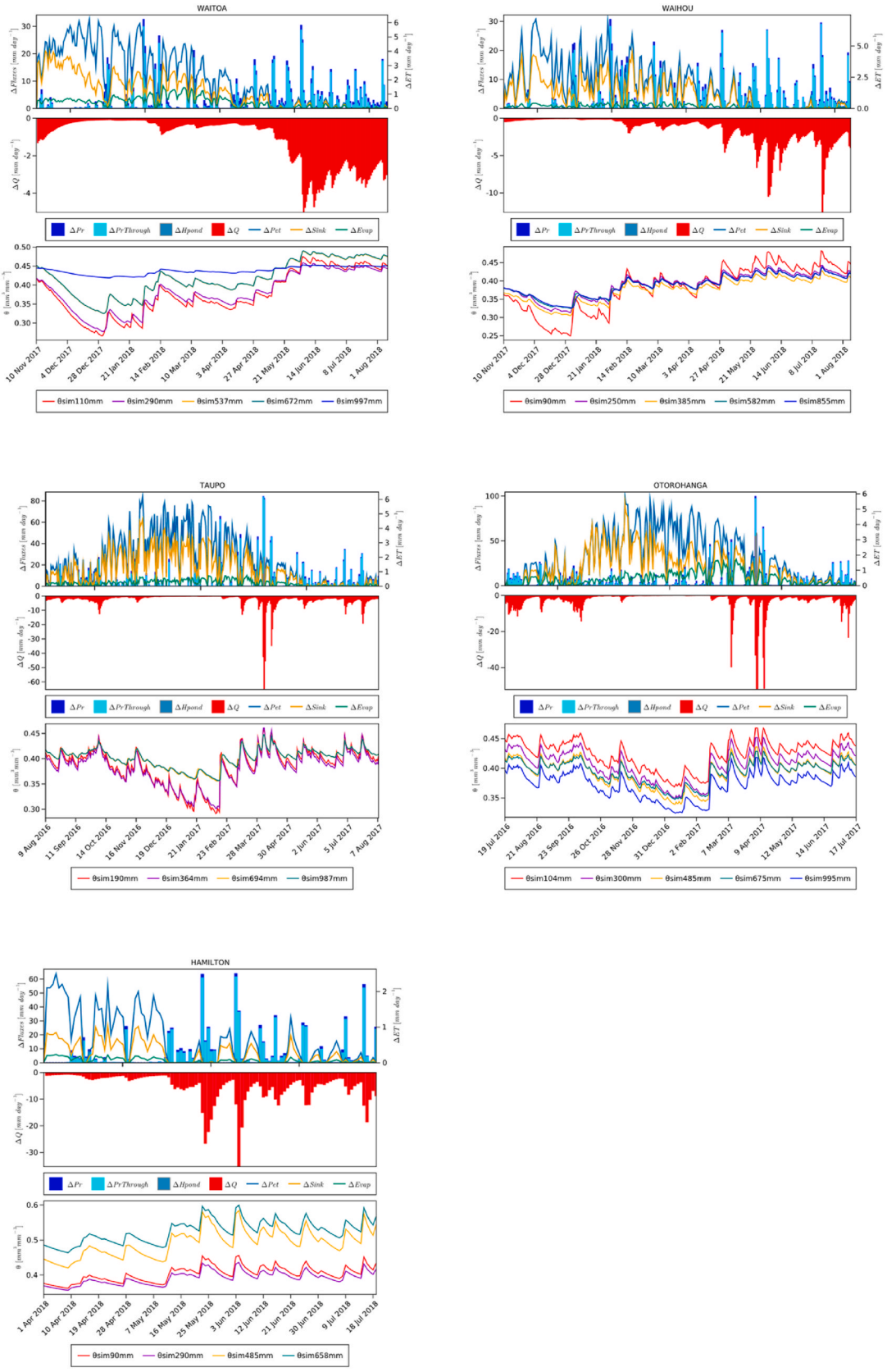

Fig. 4. Simulated water balance components (precipitation, evaporation, and drainage) with HyPix for the experimental sites. ΔQ, ponding depth ΔH_{pond} [Eq. (10)], throughfall precipitation $\Delta Pr_{\text{through}}$ [Eq. (75)], potential evapotranspiration ΔPet [Eq. (68)], sink term $\Delta Sink$ [Eq. (80)], evaporation $\Delta Evap$ [Eq. (81)], and soil water content at depths incremented down the soil profile.

Table 5
Normalized overall water balance (WB^* [%]) and efficiency (E_{ff} [day^{-1}]) of simulations for the different options implemented in HyPix with a vertical discretization of 20 mm in the root zone and 50 mm below the root zone. The novel adaptive time-stepping management based on ψ for solving the RRE is used. Options for controlling the Newton–Raphson step include: a modified iteration criterion for initially dry conditions from Zha et al. (2017) (*Dry method*), and the *smoothing criteria with* Ω (constant or dynamic).

Dry method	Ω	Waitoa		Waihou		Taupō		Otorohanga		Hamilton	
		WB^{η} [%]	E_{ff} [day^{-1}]	WB^{η} [%]	E_{ff} [day^{-1}]	WB^{η} [%]	E_{ff} [day^{-1}]	WB^{η} [%]	E_{ff} [day^{-1}]	WB^{η} [%]	E_{ff} [day^{-1}]
NO	Const.	0.55	161	0.27	180	0.43	170	0.30	164	0.48	152
YES	Const.	0.55	161	0.27	180	0.43	170	0.30	164	0.48	152
NO	Dyna.	$<10^{-4}$	45	$<10^{-4}$	49	$<10^{-4}$	50	$<10^{-4}$	49	$<10^{-4}$	51
YES	Dyna.	$<10^{-4}$	45	$<10^{-4}$	49	$<10^{-4}$	50	$<10^{-4}$	49	$<10^{-4}$	51

bucket rain gauge recording at 0.2 mm rain depth resolution. *Potential evapotranspiration*, ΔPet [L], was derived from the New Zealand Virtual Climate Stations (VCS) network (Tait et al., 2006; Tait, 2008), with estimates based on the spatial interpolation of actual data observations made at climate stations located around the country (Tait, 2010). Soil water content, θ [L^3 L^{-3}], was monitored at five depth increments to 1000 mm depth, with minor increment variation between soils to reflect soil layer differences.

For the five sites, HyPix uses a 2-month period of warm up. The yearly average *precipitation* and *potential evapotranspiration* using representative wet and dry periods from 6 months' data are shown in Table 4.

4. Results

The results are organized as follows. In section 4.1 we compare *θ-profile* computed with HyPix and HYDRUS by disabling the sink term for the five test cases described in section 3.1. Not including the sink term causes a sharper ψ wetting front and therefore is a more challenging problem for the solver of the RRE, since including the sink term attenuates the wetting front. Moreover, the sink terms computed in HYDRUS are different from the one computed in HyPix. In section 4.2 we run HyPix using data from contrasting experimental sites (section 3.2) and include the sink term to illustrate the benefits of the recommended HyPix options derived in the test cases. In section 5.1 we recommend HyPix options such that, in order of priority, the results are stable (converge), are accurate, have a good water balance, and are efficient.

4.1. Validation of HyPix with HYDRUS using synthetic test cases

HyPix simulations were derived using the *dynamic* Ω (section 2.3.4.3), the *dry method* (section 2.3.4.4) for controlling the NR steps, as well as the *time-stepping management based on* ψ for solving the RRE (section 2.3.3.2). The comparison of the θ-profiles at different times computed by HYDRUS (solid line) and HyPix (dashed line), respectively, for the five test cases described in section 3.1 are shown in Fig. 3. The different colours indicate the time since the beginning of each simulation and are evenly spaced (red, purple, and yellow) until the total time of simulation (blue). As shown in Fig. 3, the matching in θ-profile between HYDRUS and HyPix is excellent, with almost indistinguishable θ-profiles throughout the time for each of the five test cases. This is also confirmed in Table 3, with *RMSE* [Eq. (37)] values very close to zero (RMSE $\leq$1.8 10^{-2}) and *NSE* [Eq. (38)] values close to 1 (NSE $\geq$ 0.93) computed between simulated θ-profiles with HYDRUS and HyPix models. The drainage from the bottom cell during the total time of simulation ($\Delta Q^{N_{IT}}_{N+\frac{1}{2}}$) computed with HyPix and HYDRUS is similar, as shown in Table 3. Therefore, the algorithm implemented in HyPix is as robust as the one implemented in HYDRUS.

4.2. HyPix tested with experimental sites

In this section we run HyPix with experimental data (section 3.2) using time series of climatic variables, soil information from the five contrasting experimental sites, and the sink term of the RRE to illustrate the benefits of the recommended HyPix options. In the previous section it was shown that for the five test cases HyPix converged successfully using the physical *time-stepping-ψ* (section 2.3.3.2) and the *dynamic* Ω algorithm to control the NR step (section 2.3.4.3) in combination with the *dry method* derived from Zha et al. (2017) (section 2.3.4).

In most applications solving the RRE for hydrological modelling, coarse vertical resolutions are used to decrease the computational burden. An essential element of the numerical solution of the RRE is that the solution converges as the spatial resolution increases. To simulate hydrological fluxes accurately, small vertical cell sizes, in the order of 10 mm, are required near the soil surface but not throughout the soil column (Downer and Ogden, 2004). The performance of HyPix, which uses the NR algorithm, was tested using different discretization ranging from 10 to 100 mm (data not shown). To evaluate the model performance using the different options implemented in HyPix we selected a vertical discretization of $\Delta Z_{uz} = 20$ mm and $\Delta Z_{lz} = 50$ mm, where ΔZ_{uz} is the discretization of the upper zone in the root zone, taken here as $Z \leq$ 500 mm, and ΔZ_{lz} is the discretization of the lower zone below the root zone. The maximum errors of the water balance between the finest discretization ($\Delta Z_{uz} = 10$ mm and $\Delta Z_{lz} = 10$ mm) compared to a coarser discretization used to illustrate the model performance, with the different options ($\Delta Z_{uz} = 20$ mm and $\Delta Z_{lz} = 50$ mm) for Δ*Drainage* and Δ*Sink* are below 0.03% for all sites described in section 3.2.

The yearly water balance for the five experimental sites is shown in Table 4 and the plots are shown in Fig. 4. The rainfall interception algorithm uses vegetation parameters (section 3.2.2), which are described in Appendix. The closure of the simulated water balance is shown by the normalized overall excellent water balance $WB^{\eta} < 10^{-4}$ [Eq. (35)].

For each of the five experimental sites Table 5 evaluates HyPix performance through WB^{η} and E_{ff} of the simulations by **(a)** using/not using the *dry method*, and **(b)** using the *smoothing criteria with* Ω either constant or dynamic. With the recommended options described in the last row we obtain excellent results with $WB^{\eta} < 10^{-4}$ [%] and $E_{ff} \leq 66$ [day^{-1}]. The benefits of using the *dry method* and the *dynamic smoothing* criterion are discussed in section 5.

5. Discussion

To concisely interpret the significance of the algorithms implemented in HyPix, we present in this section the recommended HyPix options as well as the pros and cons of each of them as evidenced by the results.

5.1. Recommended HyPix options

The results described in Fig. 3 and Table 5 were derived using the time-step controlled by using the physical *time-stepping-ψ* (section 2.3.3.2), and the NR step is managed using the *dynamic* Ω (section 2.3.4.3) in combination with the *dry method* derived from Zha et al. (2017) (section 2.3.4). We did not use the *absolute convergence criterion* (section 2.3.4.1) for reasons discussed in section 5.5. We discuss the

recommended HyPix options derived from the synthetic test cases (section 4.1) and the experimental data set (section 4.2) having the greatest probability to be successful in most cases such that, in order of priority, the results are stable (successful converge), are accurate, have a good water balance, and are efficient.

As described in Table 5, for the four test cases (except for **TC5**), the accuracy of the HyPix *WB* is greater than that for HYDRUS. The E_{ff} of HyPix for **TC1** (coarse soils) is 44 times more efficient due to the implementation of *time-stepping-ψ*, and the *dynamic Ω* in combination with the *dry methods*. HyPix was also slightly more efficient in **TC2** using the same soils as in **TC1**. The E_{ff} in **TC3** with HYDRUS and HyPix are quite similar, but HyPix was slightly more efficient in **TC4**. For the modelling of impermeable layers, **TC5**, HYDRUS was five times more efficient than HyPix (this is further discussed in section 5.6).

5.2. Benefits of time-stepping-ψ compared to time-stepping-θ

By using the HyPix parameters described in Table 1, we found that for **TC1** and **TC2** (coarse texture soils), the model failed to converge when using as an option the traditional *time-stepping-θ*. Nonetheless, these cases were successful when using the *time-stepping-ψ*. For the other test cases the *time-stepping-θ* was successful and marginally more efficient in the *WB* and E_{ff} (results not shown) than the *time-stepping-ψ*.

The *time-stepping-ψ* is more accurate than the *time-stepping-θ*, particularly for coarse texture soils, because, the *time-stepping-ψ* reduces ΔT when the soil is close to saturation by reducing $\Delta\theta^{t}_{\max_i}$ [Eq. (25)]. This is important because close to saturation we have $\partial\theta/\partial\psi \simeq 1$, which could lead the NR step to go to infinity.

Therefore, the adaptive time-stepping management for solving the RRE based on ψ is the recommended option for HyPix because it enables the success of convergence and accuracy for all soil types and boundary conditions.

5.3. Benefits of the dry method

The use of the modified iteration criterion for initially dry conditions from Zha et al. (2017) (section 2.3.4.4) enables **TC1** and **TC2** to converge using large $\Delta\theta_{\max}$ (Table 1). Nevertheless, the dry method had no effect for the other finer-texture test cases. Similar results were found in Table 5 by using real test cases with finer texture soils. The results are in line with those of Zha et al. (2017), who found that the *dry methods* only benefited coarse texture soils (with small σ) and when infiltration occurs into initially dry conditions.

The dry method successfully detects if there is any oscillation at the dry end of the *θ(ψ)* curve caused by infiltration into dry soils. If this occurs, then the next iteration is computed from $\partial\theta/\partial\psi$ [Eq. (3)]. In order to apply the *dry method*, $\psi_{\mathrm{dry}}(\sigma)$ and $\psi_{\mathrm{wet}}(\sigma)$ [Eq. (39)] need to be computed. We recommend applying the *dry method* for all soils because it gets activated only when oscillation occurs at the dry end of the *θ(ψ)* curve.

5.4. Benefits of dynamic Ω

The benefits of the novel physical dynamic *Ω* smoothing criterion (section 2.3.4.3) for controlling the NR steps compared to the traditional constant *Ω* (section 2.3.4.2) was evaluated with the experimental data (section 4.2) under variable fluxes and sink term using the universal HyPix parameters described in Table 1. The novel dynamic *Ω* smoothing criterion outperforms in accuracy and efficiency the smoothing criterion with constant *Ω* for all sites. The use of the *dynamic Ω* dramatically reduces WB^{η} [Eq. (35)] by three orders of magnitude, and increases E_{ff} threefold.

This is because the NR step reduces automatically during iteration when large $\left|\theta(\psi_i^{t,k+1}) - \theta(\psi_i^{t,k})\right|$ is encountered compared to $\Delta\theta^{t,k}_{\max}$ (Eq. (25) computed from *time-stepping-ψ*). The convergence rate is slowed but the success rate of convergence is increased. The other benefit of the dynamic *Ω* is that it does not require any extra parameters. We therefore strongly recommend the *dynamic Ω smoothing criterion.*

5.5. Non benefits of the absolute convergence criterion

For **TC1** and **TC2** (*sandy loam soils*) there were some minor improvements in the *WB* and E_{ff} using the *absolute convergence criterion* (section 2.3.4.1) to control the NR step (results not shown). Nevertheless, when using the *absolute convergence criterion* for finer texture soils such as **TC3**, **TC4** and **TC5**, it failed to converge.

The *absolute convergence criterion*, $\Delta\ln\psi_{\max_i} \geqslant \left|\ln(\psi_i^{t,k}) - \ln(\psi_i^{t,k-1})\right|$, fails to improve the results because the *dynamic Ω* accurately controls the NR step considering a smoother transition in the overall NR method. Therefore, the use of the *absolute convergence criterion* is not recommended.

5.6. Impermeable layers

In **TC5** we model saturating a soil profile from the top with an impermeable layer at the bottom. HyPix is successful in obtaining excellent water balance, being four orders of magnitude more accurate that HYDRUS and null drainage at the bottom while HYDRUS has some drainage at the bottom. This would explain why HyPix is considerably less efficient for this case than HYDRUS, because with the selected parameters HyPix has higher accuracy.

6. Conclusions

The newly developed open-source **Hy**drological **Pix**el model, HyPix, written in the fast and flexible Julia language efficiently solves the mixed form of the RRE. HyPix uses a *cell-centred, finite-volume* scheme for the spatial discretization, with an *implicit Euler scheme* for the temporal discretization, by using the *weighted average* inter-cell hydraulic conductivity. HyPix includes the following modules: **(a)** *rainfall interception*, **(b)** *root water uptake* with compensation algorithm and root growth, **(c)** *soil evaporation*, and **(d)** *ponding*, and **(e)** *runoff* using a novel method for computing sorptivity. HyPix includes a wide range of top and boundary conditions (flux, pressure, free).

The drawback of using the NR method for solving the RRE is that every configuration (e.g., changing the inter-cell hydraulic conductivity) requires reprogramming the derivatives (Appendix). HyPix implements an option to solve the derivatives numerically (section 2.3.2), enabling the RRE to be modified by changing only a few lines of code. Numerically calculating derivatives was found to be as accurate as deriving the derivatives mathematically, and only 10–25% slower.

For controlling the Newton–Raphson steps, HyPix incorporates several options where it is demonstrated that the recommended novel physical smoothing criterion for controlling the Newton–Raphson step with dynamic *Ω* improves not only the model performance but also its accuracy compared to using the traditional absolute convergence criterion.

For controlling the time-step, the physical *time-step management based on Δθ* (Kirkland et al., 1992; Ross, 2003) was specifically designed to solve RRE based on *θ*. Therefore, we adapted the time-step management so that it is specifically designed to solve RRE based on *ψ* without introducing further parameters. The novel time-step management requires only one parameter and was found to be more efficient than the traditional time-step management.

The well-established hydrological model HYDRUS was used to validate HyPix. The comparison of both models shows a remarkable agreement, confirming the validity of the algorithms implemented in HyPix. Even for challenging conditions HyPix can provide accurate and reliable results using the recommended standard options. Moreover, the

algorithm developed in HyPix generates results more efficiently that the one used in HYDRUS, particularly for coarse texture soils. An additional benefit of HyPix is its simplicity to use because it requires only eight parameters (HYDRUS has 13 fitting parameters), and most of them can be safely kept to the recommended value described in Table 1.

The stability and robustness of the solution of the RRE in HyPix enables it to be used for inverse modelling.

Software/Data availability

The HyPix model source code and the test cases can be downloaded from https://github.com/manaakiwhenua/SoilWater_ToolBox.jl and is open source under the GP-3.0 License. HyPix is written in the open-source Julia programming language and can be run under multiple platforms https://julialang.org/downloads. Access to the experimental field data require permission from Environment Canterbury (https://www.ecan.govt.nz/) while the sites and the latest monitoring data can be viewed at https://www.waikatoregion.govt.nz/environment/envirohub/environmental-maps-and-data?dt=Soil+Moisture&af=latestValue&a=latest.

HyPix is part of a set of interlinked modules implemented into the SoilWater-ToolBox ecosystem led by J.A.P Pollacco from Manaaki Whenua – Landcare Research in New Zealand and J. Fernández-Gálvez from the University of Granada in Spain. The preliminary objective of the SoilWater-ToolBox is to derive the soil hydraulic parameters by using wide range of cost-effective methods. The estimated hydraulic parameters can be directly implemented into HyPix to compute the soil water budget. The SoilWater-ToolBox enables the comparison and sensitivity analyses of the hydraulic parameters computed from different methods on the soil water fluxes. The following modules are currently included into the SoilWater-ToolBox:

- **Intergranular Mixing Particle size distribution module:** derives unimodal hydraulic parameters by using particle size distribution (Pollacco et al., 2020);
- **General Beerkan Estimation of Soil Transfer parameters module:** derives the unimodal hydraulic parameters from single ring infiltration experiments (Fernández-Gálvez et al., 2019);
- **Sorptivity module:** a novel computation of sorptivity used in the General Beerkan Estimation of Soil Transfer parameters method (Lassabatere et al., 2021, 2022);
- **Saturated hydraulic conductivity module derived from unimodal and bimodal $\theta(\psi)$** (Pollacco et al., 2013b, 2017);
- **Inverse module which inverts hydraulic parameters from θ time series** (Pollacco et al., 2022);
- **Reduce uniqueness module of a physical bimodal soil Kosugi hydraulic parameters** from inverse modelling (Fernández-Gálvez et al., 2021) using water retention and/or unsaturated hydraulic conductivity data directly measured in the laboratory or indirectly obtained from inverting θ time series.

Declaration of competing interest

The authors declare that they have no known competing financial interests or personal relationships that could appear to influence the work reported in this paper.

Acknowledgements

This research was supported by the 'Winning Against Wildings' research programme, funded by the New Zealand Ministry of Business, Innovation and Employment, and through the *Manaaki Whenua*-led 'Next Generation S-map' research programme. We would like to thank Justin Wyatt, Waikato Regional Council, New Zealand for providing monitored data for the field sites. Funding for open access charge: Universidad de Granada / CBUA.

Appendix

Jacobian matrices

The *Newton–Raphson* solution requires the Jacobian matrix, which can be written in a matrix form as an example with N_{iZ} depths. The numerical discretization is a tridiagonal non-linear set of equations, which needs to be solved for $[{\psi_{iZ}}^{iT,k+1} - \psi_{iZ}^{iT,K}]$ for every time-step and for every iteration, k.

$$\begin{matrix} i=1 \\ i=2 \\ i=3 \\ \dots \\ i=N-1 \\ i=N \end{matrix}\begin{bmatrix} \frac{\partial R_1^{t,k}}{\partial \psi_1^t} & \frac{\partial R_1^{t,k}}{\partial \psi_2^t} & 0 & 0 & 0 \\ \frac{\partial R_2^{t,k}}{\partial \psi_1^t} & \frac{\partial R_2^{t,k}}{\partial \psi_2^t} & \frac{\partial R_2^{t,k}}{\partial \psi_3^t} & 0 & 0 \\ 0 & \frac{\partial R_3^{t,k}}{\partial \psi_2^t} & \frac{\partial R_3^{t,k}}{\partial \psi_3^t} & \frac{\partial R_3^{t,k}}{\partial \psi_4^t} & 0 \\ \dots & \dots & \dots & \dots & \dots \\ 0 & 0 & \frac{\partial R_{N-1}^{t,k}}{\partial \psi_{N-2}^t} & \frac{\partial R_{N-1}^{t,k}}{\partial \psi_{N-1}^t} & \frac{\partial R_{N-1}^{t,k}}{\partial \psi_N^{t+1}} \\ 0 & 0 & 0 & \frac{\partial R_N^{t,k}}{\partial \psi_{N-1}^t} & \frac{\partial R_N^{t,k}}{\partial \psi_N^t} \end{bmatrix} \cdot \begin{bmatrix} \psi_1^{t,k+1} - \psi_1^{t,k} \\ \psi_2^{t,k+1} - \psi_2^{t,k} \\ \psi_3^{t,k+1} - \psi_3^{t,k} \\ \dots \\ \psi_{N-1}^{t,k+1} - \psi_{N-1}^{t,k} \\ \psi_N^{t,k+1} - \psi_N^{t,k} \end{bmatrix} = \begin{bmatrix} -R\left(\psi_1^{t,k}\right) \\ -R\left(\psi_2^{t,k}\right) \\ -R\left(\psi_3^{t,k}\right) \\ \dots \\ -R\left(\psi_{N-1}^{t,k}\right) \\ -R\left(\psi_N^{t,k}\right) \end{bmatrix} \tag{40}$$

The solution of these sets takes place by means of the *tridiagonal function*, which is an effective modification of the Gauss algorithm for the solution of a tridiagonal linear set of equations. In Julia we use the efficient *tridiagonal function* to solve the matrix. The derivatives of R are shown below.

Derivatives of residuals

Julia		$i = 1$	Eq.
$\partial R \partial \Psi \triangle$	$\frac{\partial R_1^{t,k}}{\partial \psi_0^t}$	Not applicable	(41)
$\partial R \partial \Psi$	$\frac{\partial R_1^{t,k}}{\partial \psi_1^t}$	Same as $2 \leq i \leq N-1$	(42)
$\partial R \partial \Psi \nabla$	$\frac{\partial R_1^{t,k}}{\partial \psi_2^t}$	Same as $2 \leq i \leq N-1$	(43)
		$\mathbf{2 \leq i \leq N\text{-}1}$	
$\partial R \partial \Psi \triangle$	$\frac{\partial R_i^{t,k}}{\partial \psi_{i-1}^{t,1}}$	$-\Delta t \frac{\partial Q_i^t}{\partial \psi_{i-1}^t}$	(44)
$\partial R \partial \Psi$	$\frac{\partial R_i^{t,k}}{\partial \psi_i^t}$	$\Delta Zi\left[\frac{\partial \theta_i(\psi_i^t)}{\partial \psi_i^t}\left[1 - \frac{S_o}{\theta_s}(\psi_i^{t-1} - \psi_i^t)\right] - \frac{S_o}{\theta_s}\theta_i(\psi_i^t)\right] - \Delta t\left(\frac{\partial Q_{i-1/2}^t}{\partial \psi_i^t} - \frac{\partial Q_{i+1/2}^t}{\partial \psi_i^t}\right)$	(45)
$\partial R \partial \Psi \nabla$	$\frac{\partial R_i^{t,k}}{\partial \psi_{i+1}^t}$	$\Delta t \frac{\partial Q_{i+1/2}^t}{\partial \psi_{i+1}^t}$	(46)
		$\boldsymbol{i = N}$	
$\partial R \partial \Psi \triangle$	$\frac{\partial R_N^{t,k}}{\partial \psi_{N-1}^t}$	Same as $2 \leq i \leq N-1$	(47)
$\partial R \partial \Psi$	$\frac{\partial R_N^{t,k}}{\partial \psi_N^t}$	Same as $2 \leq i \leq N-1$	(48)
$\partial R \partial \Psi \nabla$	$\frac{\partial R_N^{t,k}}{\partial \psi_{N+1}^t}$	Not applicable	(49)

Derivatives of Q

Julia		$i = 1$	Eq.
$\partial Q \partial \Psi \triangle$	$\frac{\partial Q_{1/2}^t}{\partial \psi_0^t}$	Not applicable	(50)
$\partial Q \partial \Psi$	$\frac{\partial Q_{1/2}^t}{\partial \psi_1^t}$	Flux top boundary condition $= 0$	(51)
		Prescribed top pressure boundary condition $\left[\frac{\psi_{top}^t - \psi_1^t}{\frac{\Delta Z_1}{2}} + \cos\alpha\right]\frac{\partial K_1(\psi_1^t)}{\partial \psi_1^t} - \frac{K_1(\psi_1^t)}{\frac{\Delta Z_1}{2}}$	(52)
$\partial Q \nabla \partial \Psi$	$\frac{\partial Q_{1+1/2}^t}{\partial \psi_i^t}$	Same as for $2 \leq i \leq N$	(53)
$\partial Q \nabla \partial \Psi \nabla$	$\frac{\partial Q_{1+1/2}^{t+1}}{\partial \psi_2^{t+1}}$	Same as for $2 \leq i \leq N$	(54)
Julia		$\mathbf{2 \leq i \leq N\text{-}1}$	
$\partial Q \partial \Psi \triangle$	$\frac{\partial Q_{i-1/2}^t}{\partial \psi_{i-1}^t}$	$[1 - w_i]\left[\frac{\psi_{i-1}^t - \psi_i^t}{\Delta Z_{i-1/2}} + \cos\alpha\right]\frac{\partial K_{i-1}(\psi_{i-1}^t)}{\partial \psi_{i-1}^t} + \frac{w_i[K_i(\psi_i^t)] + [1 - w_i][K_{i-1}(\psi_{i-1}^t)]}{\Delta Z_{i-1/2}}$	(55)
$\partial Q \partial \Psi$	$\frac{\partial Q_{i-1/2}^t}{\partial \psi_i^t}$	$w_i\left[\frac{\psi_{i-1}^t - \psi_i^t}{\Delta Z_{i-1/2}} + \cos\alpha\right]\frac{\partial K_i(\psi_i^t)}{\partial \psi_i^t} - \frac{w_i[K_i(\psi_i^t)] + [1 - w_i][K_{i-1}(\psi_{i-1}^t)]}{\Delta Z_{i-1/2}}$	(56)
$\partial Q \nabla \partial \Psi$	$\frac{\partial Q_{i+1/2}^t}{\partial \psi_i^t}$	$[1 - w_{i+1}]\left[\frac{\psi_i^t - \psi_{i+1}^t}{\Delta Z_{i+1/2}} + \cos\alpha\right]\frac{\partial K_i(\psi_i^t)}{\partial \psi_i^t} + \frac{w_{i+1}[K_{i+1}(\psi_{i+1}^t)] + [1 - w_{i+1}][K_i(\psi_i^t)]}{\Delta Z_{i+1/2}}$	(57)
$\partial Q \nabla \partial \Psi \nabla$	$\frac{\partial Q_{i+1/2}^t}{\partial \psi_{i+1}^t}$	$w_{i+1}\left[\frac{\psi_i^t - \psi_{i+1}^t}{\Delta Z_{i+1/2}} + \cos\alpha\right]\frac{\partial K_{i+1}(\psi_{i+1}^t)}{\partial \psi_{i+1}^t} - \frac{w_{i+1}[K_{i+1}(\psi_{i+1}^t)] + [1 - w_{i+1}][K_i(\psi_i^t)]}{\Delta Z_{i+1/2}}$	(58)
Julia		$\boldsymbol{i = N}$ **(recharge)**	
$\partial Q \partial \Psi \triangle$	$\frac{\partial Q_{N-1/2}^t}{\partial \psi_{N-1}^t}$	Same as for $2 \leq i++N-1$	(59)
$\partial Q \partial \Psi$	$\frac{\partial Q_{N-1/2}^t}{\partial \psi_N^t}$	Same as for $2 \leq i \leq N-1$	(60)
$\partial Q \nabla \partial \Psi$	$\frac{\partial Q_{N+1/2}^t}{\partial \psi_N^t}$	Free drainage bottom boundary condition $\frac{\partial K_N(\psi_N^t)}{\partial \psi_N^t}\cos\alpha$	(61)
		Prescribed bottom pressure boundary condition $\left[\frac{\psi_N^t - \psi_{\text{bot}}^t}{\frac{\Delta Z_N}{2}} + \cos\alpha\right]\frac{\partial K_N(\psi_N^t)}{\partial \psi_N^t} + \frac{K_N(\psi_N^t)}{\frac{\Delta Z_N}{2}}$	(62)
		Bottom boundary condition $= 0$	(63)
	$\frac{\partial Q_{N+1/2}^{t+1}}{\partial \psi_{N+1}^{t+1}}$	Not applicable as $\psi_{N+1}^{t+1} = \text{Const}$	(64)

Potential evapotranspiration

The *potential evapotranspiration* depth, ΔPet [L], for a time-step ΔT is computed using the Penman–Monteith equation. Input variables used the estimates derived from the New Zealand Virtual Climate Stations network (VCS), which are based on the spatial interpolation of actual data observations made at climate stations located around the country (Tait et al., 2006). We assume that:

$$\Delta Pet = \Delta Pet_{\text{int}} \tag{65}$$

where ΔPet_{int} [L] is the *interception potential evaporation depth*, which is the potential evaporation from a wet canopy. The remaining energy that is not used to evaporate water from a wet canopy (e.g., periods with no rainfall) allows the *potential evapotranspiration depth*, ΔPet_{et} [L], to be computed as:

$$\Delta Pet_{\text{et}} = \Delta Pet - \Delta Evap_{\text{int}} \tag{66}$$

where $\Delta Evap_{\text{int}}$ [L] is derived from the actual energy used to evaporate water from a wet canopy.

The *potential transpiration depth* of vegetation, $\Delta Pet_{\text{transp}}$ [L], and *potential evaporation depth of soil*, ΔPet_{evap} [L], is partitioned from ΔPet_{et} by using the Beer–Lambert law, which uses as parameters the leaf area index, *LAI* [-]. *LAI* can be derived from remote sensing (Béland et al., 2014). The Beer–Lambert law assumes that the net radiation inside the canopy decreases exponentially. Therefore, the partitioning of ΔPet_{et} is given by:

$$\Delta Pet_{\text{evap}} = \Delta Pet_{\text{et}} e^{-K_g LAI} \tag{67}$$

$$\Delta Pet_{\text{transp}} = \Delta Pet_{\text{et}} - \Delta Pet_{\text{evap}} \tag{68}$$

where the *extinction coefficient for solar radiation*, K_g [-], is set to 0.5 (e.g., Varado et al., 2006).

Rainfall interception

The parsimonious physically based interception model is an improvement made by Pollacco et al. (2013a). The following interception model uses *potential evaporation of a wet canopy* ΔPet_{int}, [Eq. (65)], *LAI* [-], and *extinction coefficient for solar radiation*, K_g [-] set to 0.5. The *gross precipitation depth* that falls on top of a canopy, ΔPr [L], is partitioned following Rutter et al. (1971) as:

$$\Delta Pr = \Delta Pr_{\text{int}} + \Delta Pr_{\text{ground}} \tag{69}$$

where $\Delta Pr_{\text{ground}}$ [L] is the fraction of precipitation reaching the soil surface through gaps in the canopy, and ΔPr_{int} [L] is the *intercepted precipitation depth*. They are computed as:

$$\begin{cases} \Delta Pr_{\text{ground}} = G_{\text{apFrac}} \Delta Pr \\ \Delta Pr_{\text{int}} = \left[1 - G_{\text{apFrac}}\right] \Delta Pr \end{cases} \tag{70}$$

where the gap fraction, G_{apFrac} [-], is calculated similarly to Eq. (67):

$$G_{\text{apFrac}} = 1 - e^{-K_g LAI} \tag{71}$$

The foliage of the canopy is considered as water storage filled up to depth *Sint* [L], *with a saturated storage capacity*, $Sint_{\text{sat}}$ [L]. When the canopy is fully saturated ($Sint = Sint_{\text{sat}}$), then any excess of ΔPr_{int} overflows, ΔPr_{over} [L], to the soil surface. The amount of water that reaches the soil surface is the *throughfall precipitation* [L]:

$$\Delta Pr_{\text{through}} = \Delta Pr_{\text{ground}} + \Delta Pr_{\text{over}} \tag{72}$$

The water storage of the canopy is first computed as:

$$Sint^t = Sint^{t-1} + \Delta Pr_{\text{int}} \tag{73}$$

A fraction of the water from *Sint* will be evaporated at the rate of the *actual evaporation* depth, $\Delta Evap_{\text{int}}$ [L], during and after a rainfall event. The maximum quantity of water that can be evaporated from a wet canopy during a time-step is computed according to Deardorff (1978), which assumes that $\Delta Evap_{\text{int}}$ is proportional to the fraction of the canopy that is wet:

$$\Delta Evap_{\text{int}} = \Delta Pet_{\text{int}} \left[\frac{\min\{Sint^t; Sint_{\text{sat}}\}}{Sint_{\text{sat}}} \right]^{Pevap_{\text{int}}} \tag{74}$$

where $Pevap_{\text{int}}$ [-] is a constant parameter for which Deardorff (1978) gives a constant value of 2/3.

ΔPr_{over} is computed as:

$$\begin{cases} \Delta Pr_{\text{over}} = \min\left\{Sint^{t-1} + \Delta Pr_{\text{int}} - \Delta Evap_{\text{int}} - S_{\text{sat}};\ 0\right\} \\ Sint^{\text{t}} = \min\left\{Sint^{t-1} + \Delta Pr_{\text{int}} - \Delta Evap_{\text{int}} - \Delta Pr_{\text{over}};\ 0\right\} \end{cases} \tag{75}$$

Rainfall interception of gross rainfall loss, *InterceptionLoss* [0–1] is computed by:

$$InterceptionLoss = 1 - \frac{\sum_{t=1}^{N_t} \Delta Pr^t_{\text{through}}}{\sum_{t=1}^{N_t} \Delta Pr^t} \tag{76}$$

In the HyPix model the rainfall interception module is run first, followed by the computation of $\Delta Pet_{\text{transp}}$ and ΔPet_{evap}, as described in Appendix.

Sink term

The sink term, $\Delta Sink$, described in Eq. (5) is a function of the *soil evaporation depth*, $\Delta Evap$ [L] [Eq. (78)], and the *root water uptake depth* of the vegetation, ΔRwu [L], [Eq. (79)]:

$$\Delta Sink = \Delta Evap + \Delta Rwu \tag{77}$$

evaporation: ΔEvap

The evaporation model based on Romano and Giudici (2009) and adapted by Pollacco and Mohanty (2012) is computed as:

$$\Delta Evap = \Delta Pet_{\text{evap}} Se_1 \tag{78}$$

where Se_1 [0–1] [-] refers to the *effective soil water content* defined in Eq. (1) for the top cell, and ΔPet_{evap} [L] is the *potential evaporation* depth computed with the Beer–Lambert law [Eq. (67)].

Root water uptake: ΔRwu

The root water uptake computes the volume of water removed per unit time from a unit volume of soil in the root zone and is computed for each cell i:

$$\Delta Rwu_i = \min\left\{K_c\ \Delta Pet_{\text{transp}}\ \Delta Rdf_i\ FwaterStress_i\ RootComp_i\ ;\ \Delta Z\left[\theta_i^t - \theta r_i^t\right]\right\} \tag{79}$$

where ΔRwu [L] is the *root water uptake depth*; K_c [-] is the *crop coefficient*; $\Delta Pet_{\text{transp}}$ [L] corresponds to the *potential transpiration* depth [Eq. (68)]; ΔRdf [-] refers to the percentage of roots per cell; *FwaterStress* [-] is the *water stress function* per cell, which computes the reduction of transpiration based on ψ; and *RootComp* [-] is the root compensation by enabling water uptake from deeper layers when the upper layers are depleted.

Root density function: ΔRdf

The percentage of roots per cell, i, is given by ΔRdf_i, which defines the general shape of the roots, as given by the example provided in Fig. 5. The root distribution is based on an improved empirical function of Gale and Grigal (1987), which was modified by Pollacco et al. (2008). The model requires, as parameters, solely the *maximum rooting depth*, $Z_{N\text{root}}$ [L] and the percentage of roots in the top 30 cm (other values can be taken), ΔRdf_{Top} [%]. The model compared to Gale and Grigal (1987) guarantees that the sum of $\Delta Rdf_i = 1$.

The fraction of roots, ΔRdf_i [-], for each cell, i, is computed as:

$$\Delta Rdf_i = \frac{R_d^{\,Z_{i+\frac{1}{2}}} - R_d^{\,Z_{i-\frac{1}{2}}}}{1 - R_d^{\,Z_{N\text{root}}}} \text{ with } \sum_{i=1}^{i=N\text{root}} \Delta Rdf_i = 1 \tag{80}$$

where $Z_{i-\frac{1}{2}}$ and $Z_{i+\frac{1}{2}}$ [L] are respectively the depth of the top and the bottom of cell i, as described in Fig. 1; R_d [-] is the routing distribution parameter (computed numerically from $Z_{N\text{root}}$ and ΔRdf_{Top}). R_d varies between 0.7000 and 0.9999, such that when R_d is close to 0.7, all the roots are distributed at the top, and when R_d is close to 1, the roots are evenly distributed within the root zone.

The value of R_d is computed by solving the following equation:

$$\Delta Rdf_{\text{Top}} = \frac{R_d^{\,0} - R_d^{\,30}}{1 - R_d^{\,|Z_{N\text{root}}|}} = \frac{1 - R_d^{\,30}}{1 - R_d^{\,|Z_{N\text{root}}|}} \tag{81}$$

An example of ΔRdf is provided in Fig. 5a for a soil that has equal discretization.

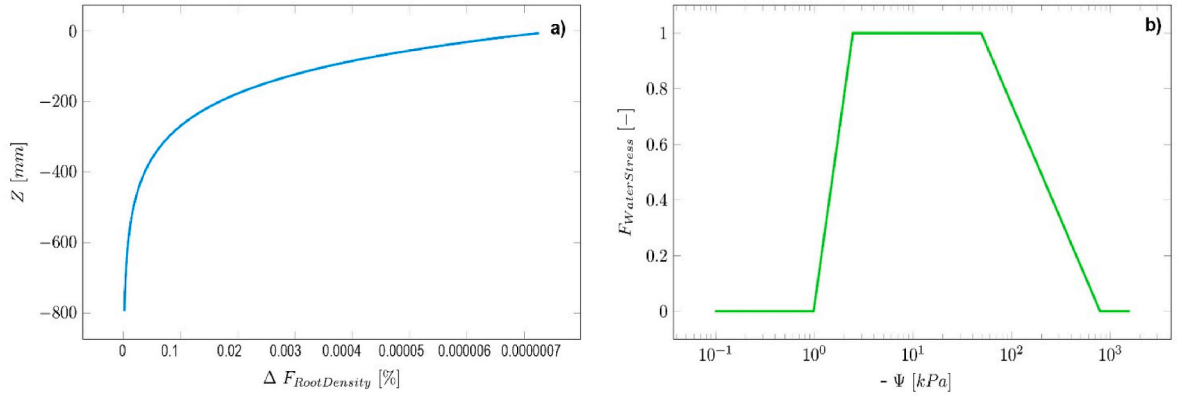

Fig. 5. Pasture grass models used for all field sites: (a) root density function plotted with depth and (b) schematic of the Feddes et al. (1978) plant water stress function.

Water stress response function: $F_{WaterStress}$

The water stress response function, $F_{WaterStress}$ [-] shown in Fig. 5b is a prescribed dimensionless function of ψ, where $(0 \leq F_{WaterStress} \leq 1)$. Following Feddes et al. (1978), $F_{WaterStress}$ is defined by using four soil water pressure values leading to a trapezoidal curve, so that:

- $F_{WaterStress} = 0$ close to saturation at a pressure greater than ψ_{Feddes1} and also above the permanent wilting point soil water pressure, ψ_{Feddes4}
- $F_{WaterStress} = 1$ between soil water pressures ψ_{Feddes2} and ψ_{Feddes3}
- for soil water pressure between ψ_{Feddes1} and ψ_{Feddes2}, $F_{WaterStress}$ increases linearly
- for soil water pressure between ψ_{Feddes3} andψ_{Feddes4}, $F_{WaterStress}$ decreases linearly.

A schematic plot of this stress response function is depicted in Fig. 5b.

Compensation mechanism: $Root_{comp}$

A *root water uptake compensation mechanism* is introduced to improve the prediction of transpiration by enabling water uptake from deeper layers when the upper layers are depleted, although the percentage of roots at deeper depth is limited. The compensation mechanism of Li et al. (2001), validated by Braud et al. (2005), is introduced. The model requires the *compensation mechanism parameter C* [-], which accounts for the general soil water content profile before computing the water uptake from individual cell *i* and is derived as:

$$\Delta RootComp_i = \frac{F_{WaterStress_i} \Delta Rdf_i^{C-1}}{\sum_{i=1}^{i=N_{root}} F_{WaterStress_i} \Delta Rdf_i^{C}} \tag{82}$$

where ΔRdf_i [Eq. (80)] is the vertical fraction of the root density function for each *i* cell [%]; $F_{WaterStress}$ is the reduction of root water uptake at pressure head ψ for every cell; and *C* is a parameter such that when $C = 1$ the model is not compensated, and when $C = 0$ the ΔRdf_i becomes constant throughout the whole root-zone depth ($I = N_{\text{root}}$). In HyPix, $C = 0.5$, as suggested by Li et al. (2001) and Braud et al. (2005).

References

Allen, R.G., Pereira, L.S., Raes, D., Smith, M., 1998. Crop Evapotranspiration-Guidelines for Computing Crop Water Requirements-FAO Irrigation and Drainage Paper 56, 300. FAO, Rome, p. D05109.

Béland, M., Widlowski, J.-L., Fournier, R.A., 2014. A model for deriving voxel-level tree leaf area density estimates from ground-based LiDAR. Environ. Model. Software 51, 184–189. https://doi.org/10.1016/j.envsoft.2013.09.034.

Belfort, B., Carrayrou, J., Lehmann, F., 2007. Implementation of Richardson extrapolation in an efficient adaptive time stepping method: applications to reactive transport and unsaturated flow in porous media. Transport Porous Media 69, 123–138. https://doi.org/10.1007/s11242-006-9090-3.

Belfort, B., Younes, A., Fahs, M., Lehmann, F., 2013. On equivalent hydraulic conductivity for oscillation–free solutions of Richard's equation. J. Hydrol. 505, 202–217. https://doi.org/10.1016/j.jhydrol.2013.09.047.

Bezanson, J., Edelman, A., Karpinski, S., Shah, V.B., 2017. Julia: a fresh approach to numerical computing. SIAM Rev. 59, 65–98. https://doi.org/10.1137/141000671.

Bisht, G., Riley, W.J., Hammond, G.E., Lorenzetti, D.M., 2018. Development and evaluation of a variably saturated flow model in the global E3SM Land Model (ELM) version 1.0. Geosci. Model Dev 11, 4085–4102. https://doi.org/10.5194/gmd-11-4085-2018.

Braud, I., Varado, N., Olioso, A., 2005. Comparison of root water uptake modules using either the surface energy balance or potential transpiration. J. Hydrol. 301, 267–286. https://doi.org/10.1016/j.jhydrol.2004.06.033.

Celia, M.A., Bouloutas, E.T., Zarba, R.L., 1990. A general mass-conservative numerical solution for the unsaturated flow equation. Water Resour. Res. 26, 1483–1496. https://doi.org/10.1029/WR026i007p01483.

Cichota, R., Kelliher, F.M., Thomas, S.M., Clemens, G., Fraser, P.M., Carrick, S., 2016. Effects of irrigation intensity on preferential solute transport in a stony soil. N. Z. J. Agric. Res. 59, 141–155. https://doi.org/10.1080/00288233.2016.1155631.

Dai, Y., Zhang, S., Yuan, H., Wei, N., 2019. Modeling variably saturated flow in stratified soils with explicit tracking of wetting front and water table locations. Water Resour. Res. 55, 7939–7963. https://doi.org/10.1029/2019WR025368.

Deardorff, 1978. Efficient prediction of ground surface temperature and moisture, with inclusion of a layer of vegetation. J. Geophys. Res. 83, 1889–1903.

Diersch, H.-J.G., Perrochet, P., 1999. On the primary variable switching technique for simulating unsaturated–saturated flows. Adv. Water Resour. 23, 271–301. https://doi.org/10.1016/S0309-1708(98)00057-8.

Downer, C.W., Ogden, F.L., 2004. Appropriate vertical discretization of Richards' equation for two-dimensional watershed-scale modelling. Hydrol. Process. 18, 1–22. https://doi.org/10.1002/hyp.1306.

Driscoll, T.A., Braun, R.J., 2017. Fundamentals of Numerical Computation. SIAM-Society for Industrial & Applied Mathematics, Philadelphia.

Evans, P.S., 1978. Plant root distribution and water use patterns of some pasture and crop species. N. Z. J. Agricult. Res. 21, 261–265. https://doi.org/10.1080/00288233.1978.10427408.

Fahs, M., Younes, A., Lehmann, F., 2009. An easy and efficient combination of the mixed finite element method and the method of lines for the resolution of Richards' equation. Environ. Model. Software 24, 1122–1126. https://doi.org/10.1016/j.envsoft.2009.02.010.

Farthing, M.W., Ogden, F.L., 2017. Numerical solution of Richards' equation: a review of advances and challenges. Soil Sci. Soc. Am. J. 81, 1257–1269. https://doi.org/10.2136/sssaj2017.02.0058.

Feddes, R.A., Kowalik, P.J., Zaradny, H., 1978. Simulation of field water use and crop yield. Simulation Monographs 189.

Fernández-Gálvez, J., Pollacco, J.A.P., Lassabatere, L., Angulo-Jaramillo, R., Carrick, S., 2019. A general Beerkan Estimation of Soil Transfer parameters method predicting hydraulic parameters of any unimodal water retention and hydraulic conductivity curves: application to the Kosugi soil hydraulic model without using particle size distribution data. Adv. Water Resour. 129, 118–130. https://doi.org/10.1016/j.advwatres.2019.05.005.

Fernández-Gálvez, J., Pollacco, J.A.P., Lilburne, L., McNeill, S., Carrick, S., Lassabatere, L., Angulo-Jaramillo, R., 2021. Deriving physical and unique bimodal soil Kosugi hydraulic parameters from inverse modelling. Adv. Water Resour. 153, 103933. https://doi.org/10.1016/j.advwatres.2021.103933.

Forsyth, P.A., Wu, Y.S., Pruess, K., 1995. Robust numerical methods for saturated-unsaturated flow with dry initial conditions in heterogeneous media. Adv. Water Resour. 18, 25–38. https://doi.org/10.1016/0309-1708(95)00020-J.

Gale, M.R., Grigal, D.F., 1987. Vertical root distributions of northern tree species in relation to successional status. Can. J. For. Res. 17, 829–834. https://doi.org/10.1139/x87-131.

Haverkamp, R., Ross, P.J., Smettem, K.R.J., Parlange, J.Y., 1994. Three-dimensional analysis of infiltration from the disc infiltrometer: 2. Physically based infiltration equation. Water Resour. Res. 30, 2931–2935. https://doi.org/10.1029/94WR01788.

Haverkamp, R., Vauclin, M., 1979. A note on estimating finite difference interblock hydraulic conductivity values for transient unsaturated flow problems. Water Resour. Res. 15, 181–187. https://doi.org/10.1029/WR015i001p00181.

Hewitt, A.E., 2010. New Zealand Soil Classification. In: Landcare Research Science Series No. 1, third ed. Manaaki Whenua Press, Lincoln, New Zealand.

Hills, R.G., Porro, I., Hudson, D.B., Wierenga, P.J., 1989. Modeling one-dimensional infiltration into very dry soils: 1. Model development and evaluation. Water Resour. Res. 25, 1259–1269. https://doi.org/10.1029/WR025i006p01259.

Jarvis, N.J., 2007. A review of non-equilibrium water flow and solute transport in soil macropores: principles, controlling factors and consequences for water quality. Eur. J. Soil Sci. 58, 523–546. https://doi.org/10.1111/j.1365-2389.2007.00915.x.

Jones, C.D., Reddy, A.D., Jeong, J., Williams, J.R., Hamilton, S.K., Hussain, M.Z., Bandaru, V., Izaurralde, R.C., 2021. Improved hydrological modeling with APEX and EPIC: model description, testing, and assessment of bioenergy producing landscape scenarios. Environ. Model. Software 143, 105111. https://doi.org/10.1016/j.envsoft.2021.105111.

Kavetski, D., Binning, P., 2004. Truncation error and stability analysis of iterative and non-iterative Thomas–Gladwell methods for first-order non-linear differential equations. Int. J. Numer. Methods Eng. 60, 2031–2043. https://doi.org/10.1002/nme.1035.

Kavetski, D., Binning, P., Sloan, S.W., 2002. Noniterative time stepping schemes with adaptive truncation error control for the solution of Richards equation: noniterative time stepping schemes. Water Resour. Res. 38, 29-1–29–10. https://doi.org/10.1029/2001WR000720.

Kavetski, D., Binning, P., Sloan, S.W., 2001. Adaptive time stepping and error control in a mass conservative numerical solution of the mixed form of Richards equation. Adv. Water Resour. 24, 595–605. https://doi.org/10.1016/S0309-1708(00)00076-2.
Kelley, C.T., 2003. Solving Nonlinear Equations with Newton's Method, Fundamentals of Algorithms. Society for Industrial and Applied Mathematics. https://doi.org/10.1137/1.9780898718898.
Kirkland, M.R., Hills, R.G., Wierenga, P.J., 1992. Algorithms for solving Richards' equation for variably saturated soils. Water Resour. Res. 28, 2049–2058. https://doi.org/10.1029/92WR00802.
Kochenderfer, M.J., Wheeler, T.A., 2019. Algorithms for Optimization. The MIT Press, Cambridge, Massachusetts.
Kosugi, K., 1994. Three-parameter lognormal distribution model for soil water retention. Water Resour. Res. 30, 891–901.
Kosugi, 1996. Lognormal Distribution Model for Unsaturated Soil Hydraulic Properties. Water Resour. Res. 32, 2697–2703. https://doi.org/10.1029/96WR01776.
Krabbenhøft, K., 2007. An alternative to primary variable switching in saturated–unsaturated flow computations. Adv. Water Resour. 30, 483–492. https://doi.org/10.1016/j.advwatres.2006.04.009.
Lassabatere, L., Peyneau, P.-E., Yilmaz, D., Pollacco, J., Fernández-Gálvez, J., Latorre, B., Moret-Fernández, D., Di Prima, S., Rahmati, M., Stewart, R.D., Abou Najm, M., Hammecker, C., Angulo-Jaramillo, R., 2021. A scaling procedure for straightforward computation of sorptivity. Hydrol. Earth Syst. Sci. 25, 5083–5104. https://doi.org/10.5194/hess-25-5083-2021.
Lassabatere, Peyneau, Yilmaz, Pollacco, Fernández-Gálvez, Latorre, Moret-Fernández, Di Prima, Rahmati, Stewart, Abou Najm, Hammecker, Angulo-Jaramillo, 2022. Mixed formulation for an easy and robust numerical computation of sorptivity. Hydrol. Earth Syst. Sci. https://doi.org/10.5194/hess-2021-633.
Lehmann, F., Ackerer, Ph, 1998. Comparison of iterative methods for improved solutions of the fluid flow equation in partially saturated porous media. Transport Porous Media 31, 275–292. https://doi.org/10.1023/A:1006555107450.
Li, K.Y., De Jong, R., Boisvert, J.B., 2001. An exponential root-water-uptake model with water stress compensation. J. Hydrol. 252, 189–204. https://doi.org/10.1016/S0022-1694(01)00456-5.
Li, Z., Özgen-Xian, I., Maina, F.Z., 2021. A mass-conservative predictor-corrector solution to the 1D Richards equation with adaptive time control. J. Hydrol. 592, 125809. https://doi.org/10.1016/j.jhydrol.2020.125809.
Maina, H.F., Ackerer, P., 2017. Ross scheme, Newton–Raphson iterative methods and time-stepping strategies for solving the mixed form of Richards' equation. Hydrol. Earth Syst. Sci. 21, 2667–2683. https://doi.org/10.5194/hess-21-2667-2017.
McLeod, M., Aislabie, J., Ryburn, J., McGill, A., 2008. Regionalizing potential for microbial bypass flow through New Zealand soils. J. Environ. Qual. 37, 1959–1967. https://doi.org/10.2134/jeq2007.0572.
Miller, C.T., Abhishek, C., Farthing, M.W., 2006. A spatially and temporally adaptive solution of Richards' equation. Adv. Water Resour. 29, 525–545. https://doi.org/10.1016/j.advwatres.2005.06.008.
Miller, C.T., Williams, G.A., Kelley, C.T., Tocci, M.D., 1998. Robust solution of Richards' equation for nonuniform porous media. Water Resour. Res. 34, 2599–2610. https://doi.org/10.1029/98WR01673.
Mualem, Y., 1976. A new model for predicting the hydraulic conductivity of unsaturated porous media. Water Resour. Res. 12, 513–522. https://doi.org/10.1029/WR012i003p00513.
National Research Council (NRC), 2001. Basic Research Opportunities in the Earth Sciences. National Academies Press, Washington, DC.
Paniconi, C., Aldama, A.A., Wood, E.F., 1991. Numerical evaluation of iterative and noniterative methods for the solution of the nonlinear Richards equation. Water Resour. Res. 27, 1147–1163. https://doi.org/10.1029/91WR00334.
Paniconi, C., Putti, M., 1994. Physically based modeling in catchment hydrology at 50: survey and outlook. Water Resour. Res. 51, 7090–7129. https://doi.org/10.1002/2015WR017780.
Parlange, J.-Y., Lisle, I., Braddock, R.D., Smith, R.E., 1982. The three-parameter infiltration equation. Soil Sci. 133, 337–341.
Perkel, J.M., 2019. Julia: come for the syntax, stay for the speed. Nature 572, 141–142. https://doi.org/10.1038/d41586-019-02310-3.
Pollacco, J.A.P., Binayak, B.P., Efstratiadis, A., 2013a. Weighted objective function selector algorithm for parameter estimation of SVAT models with remote sensing data. Water Resour. Res. 49, 6959–6978. https://doi.org/10.1002/wrcr.20554.
Pollacco, J.A.P., Braud, I., Angulo-Jaramillo, R., Saugier, B., 2008. A Linking Test that establishes if groundwater recharge can be determined by optimising vegetation parameters against soil moisture. Ann. For. Sci. 65 https://doi.org/10.1051/forest:2008046.
Pollacco, J.A.P., Fernández-Gálvez, J., Carrick, S., 2020. Improved prediction of water retention curves for fine texture soils using an intergranular mixing particle size distribution model. J. Hydrol. 584, 124597. https://doi.org/10.1016/j.jhydrol.2020.124597.
Pollacco, J.A.P., Fernandez-Galvez, J., Channa, R., Zammit, C., Ackerer, P., Belfort, B., Lassabatere, L., Raphael, A.J., Lilburne, L., Carrick, S., Peltzer, D.A., 2022. Multistep optimization of HyPix model for flexible vertical scaling of soil hydraulic parameters. Submitted to Environmental Modelling & Software.
Pollacco, J.A.P., Mohanty, B.P., 2012. Uncertainties of water fluxes in soil-vegetation-atmosphere transfer models: inverting surface soil moisture and evapotranspiration retrieved from remote sensing. Vadose Zone J. 11 https://doi.org/10.2136/vzj2011.0167.
Pollacco, J.A.P., Nasta, P., Ugalde, J.M.S., Angulo-Jaramillo, R., Lassabatere, L., Mohanty, B.P., Romano, N., 2013b. Reduction of Feasible Parameter Space of the Inverted Soil Hydraulic Parameters Sets for Kosugi Model. Soil Science SS-S-12-00268.
Pollacco, J.A.P., Webb, T., McNeill, S., Hu, W., Carrick, S., Hewitt, A., Lilburne, L., 2017. Saturated hydraulic conductivity model computed from bimodal water retention curves for a range of New Zealand soils. Hydrol. Earth Syst. Sci. 21, 2725–2737. https://doi.org/10.5194/hess-21-2725-2017.
Qi, J., Zhang, X., McCarty, G.W., Sadeghi, A.M., Cosh, M.H., Zeng, X., Gao, F., Daughtry, C.S.T., Huang, C., Lang, M.W., Arnold, J.G., 2018. Assessing the performance of a physically-based soil moisture module integrated within the Soil and Water Assessment Tool. Environ. Model. Software 109, 329–341. https://doi.org/10.1016/j.envsoft.2018.08.024.
Raats, P.A.C., 2001. Developments in soil–water physics since the mid 1960s. Geoderma 100, 355–387. https://doi.org/10.1016/S0016-7061(01)00028-3.
Radcliffe, D.E., Simunek, J., 2010. Soil Physics with HYDRUS: Modeling and Applications.
Ranatunga, K., Nation, E., Barratt, D., 2008. Review of soil water models and their applications in Australia. Environ. Model. Software 23, 1182–1206. https://doi.org/10.1016/j.envsoft.2008.02.003.
Revels, J., Lubin, M., Papamarkou, T., 2016. Forward-Mode Automatic Differentiation in Julia arXiv:1607.07892 [cs].
Richards, L.A., 1931. Capillary conduction of liquids through porous medium. J. Appl. Phys. 1, 318–333. https://doi.org/10.1063/1.1745010.
Richardson, L.F., 1922. Weather Prediction by Numerical Process.
Romano, E., Giudici, M., 2009. On the use of meteorological data to assess the evaporation from a bare soil. J. Hydrol. 372, 30–40. https://doi.org/10.1016/j.jhydrol.2009.04.003.
Ross, P.J., 2003. Modeling soil water and solute transport—fast, simplified numerical solutions. Agron. J. 95, 1352–1361. https://doi.org/10.2134/agronj2003.1352.
Rutter, A.J., Kershaw, K.A., Robins, P.C., Morton, A.J., 1971. A predictive model of rainfall interception in forests, 1. Derivation of the model from observations in a plantation of Corsican pine. Agric. Meteorol. 9, 367–384. https://doi.org/10.1016/0002-1571(71)90034-3.
Shen, C., Phanikumar, M.S., 2010. A process-based, distributed hydrologic model based on a large-scale method for surface–subsurface coupling. Adv. Water Resour. 33, 1524–1541. https://doi.org/10.1016/j.advwatres.2010.09.002.
Šimůnek, J., Genuchten, M.T. van, Šejna, M., 2016. Recent developments and applications of the HYDRUS computer software packages. Vadose Zone J. 15 https://doi.org/10.2136/vzj2016.04.0033.
Tait, A., Henderson, R., Turner, R., Zheng, X., 2006. Thin plate smoothing spline interpolation of daily rainfall for New Zealand using a climatological rainfall surface: estimation of daily rainfall over New Zealand. Int. J. Climatol. 26, 2097–2115. https://doi.org/10.1002/joc.1350.
Tait, A.B., 2008. Future projections of growing degree days and frost in New Zealand and some implications for grape growing. Weather Clim. 28, 17–36. https://doi.org/10.2307/26169696.
Tait, P.R., 2010. Valuing Agricultural Externalities in Canterbury Rivers and Streams: Three Essays. Doctoral thesis. Lincoln University, Christchurch, New Zealand, 2010.
Thomas, R.M., Gladwell, I., 1988. Variable-order variable-step algorithms for second-order systems. Part 1: the methods. Int. J. Numer. Methods Eng. 26, 39–53.
van Dam, J.C., Groenendijk, P., Hendriks, R.F.A., Kroes, J.G., 2008. Advances of modeling water flow in variably saturated soils with SWAP. Vadose Zone J. 7, 640–653. https://doi.org/10.2136/vzj2007.0060.
van Genuchten, M.T., 1980. A closed-form equation for predicting the hydraulic conductivity of unsaturated soils. Soil Sci. Soc. Am. J. 44, 892–898.
Van Housen, J., 2015. Modelling the Temporal and Spatial Variation of Evapotranspiration from Irrigated Pastures in Canterbury (Thesis). Lincoln University.
Varado, N., Braud, I., Ross, P.J., 2006. Development and assessment of an efficient vadose zone module solving the 1D Richards' equation and including root extraction by plants. J. Hydrol. 323, 258–275. https://doi.org/10.1016/j.jhydrol.2005.09.015.
Vogeler, I., Carrick, S., Cichota, R., Lilburne, L., 2019. Estimation of soil subsurface hydraulic conductivity based on inverse modelling and soil morphology. J. Hydrol. 574, 373–382. https://doi.org/10.1016/j.jhydrol.2019.04.002.
Vogeler, I., Cichota, R., 2019. Compilation of a Reference Dataset of Flux Data from Various Lysimeter Sites across New Zealand and APSIM Modelling. (No. A Plant&Food Research Report Prepared for: Landcare Research. Milestone No. 81811. Contract No. 37092. Job code: P/443063/02. PFR SPTS No. 18080.).
Wesseling, J.G., 1991. CAPSEV: Steady State Moisture Flow Theory, Program Description and User Manual (Report No. 37. Wageningen, The Netherlands, Winand Staring Centre.).
Wu, Y.-S., Forsyth, P.A., 2001. On the selection of primary variables in numerical formulation for modeling multiphase flow in porous media. J. Contam. Hydrol. 48, 277–304. https://doi.org/10.1016/s0169-7722(00)00180-7.
Zha, Y., Yang, J., Yin, L., Zhang, Y., Zeng, W., Shi, L., 2017. A modified Picard iteration scheme for overcoming numerical difficulties of simulating infiltration into dry soil. J. Hydrol. 551, 56–69. https://doi.org/10.1016/j.jhydrol.2017.05.053.
Zha, Y., Yang, J., Zeng, J., Tso, C.-H.M., Zeng, W., Shi, L., 2019. Review of numerical solution of Richardson–Richards equation for variably saturated flow in soils. WIREs Water 6, e1364. https://doi.org/10.1002/wat2.1364.